# Supplementary Information for ‘How transport systems create opportunities for social interaction’

Yitao Yang[1†], Erjian Liu[2†], Bin Jia[2], Ed Manley[1*]

[1*]School of Geography, University of Leeds, Leeds, UK.
[2]School of Systems Science, Beijing Jiaotong University, Beijing, 100044, China.

*Corresponding author(s). E-mail(s): e.j.manley@leeds.ac.uk;
Contributing authors: y.yang@leeds.ac.uk; 17120752@bjtu.edu.cn; bjia@bjtu.edu.cn;
[†]These authors contributed equally to this work.

# Contents

# List of Figures



# List of Tables

# Supplementary Information

# 1 Mobility data treatment

## 1.1 Home and workplace identification

In this study, we utilize an anonymized mobile phone dataset provided by a telecommunications company in China, covering one month (June 2023) of GPS "pings" from users who gave explicit consent. The dataset, which complies with China's Personal Information Protection Law, includes de-identified user IDs, latitudes, longitudes, and timestamps, ensuring privacy and preventing re-identification attempts. After removing duplicates and excluding users with fewer than 300 pings, our final dataset comprises 7.56 million users and roughly 4.82 billion pings.

To ensure robust inference of home and workplace locations from trajectory data, we implement a multi-stage methodology with rigorous validation. For each individual, we first detect significant stays using the DBSCAN algorithm [1]. We set the tuning parameters carefully for spatial distance of 50 meters and minimum 10 points to identify high-density clusters of trajectory points, representing visited places or stays. Once clusters are formed, we assign each cluster to the nearest Point of Interest (POI) within a predefined radius of 100 meters, ensuring that each significant stay is contextually anchored to a known venue. Clusters that are too small (fewer than 10 points) or that do not correspond to any recognized venue are discarded to minimize noise and improve data reliability. Next, we refine these significant stays by applying temporal filters to capture meaningful activities. Specifically, we exclude any stays with durations of less than 15 minutes, as such brief stops are unlikely to represent significant activities, and we also filter out stays exceeding 24 hours, which may indicate data errors. We have extracted 241 million trips for 7.56 million users. The trip characteristics in Beijing metropolitan area are shown in Supplementary Fig. 1.

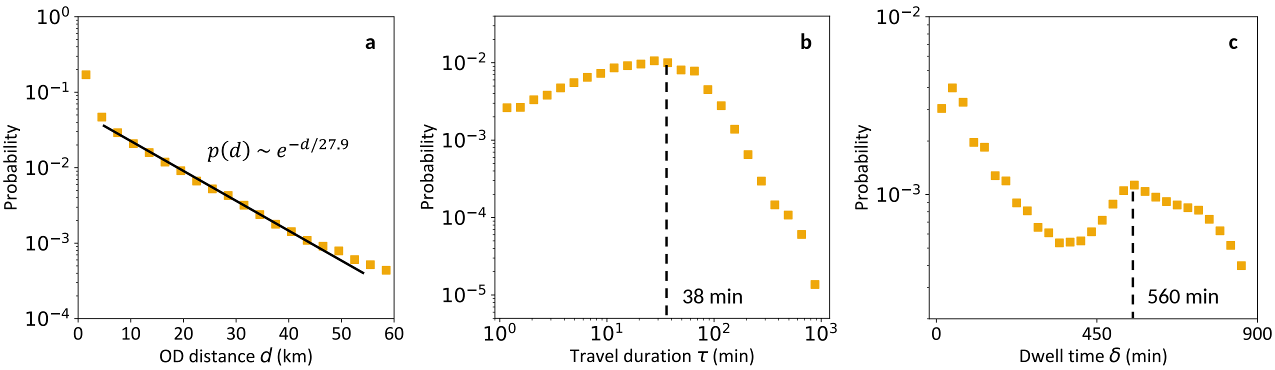


**Supplementary Figure 1 | Trip characteristics in Beijing metropolitan area. a** Distribution of trip distance $d$, which follows an exponential decay $p(d) \sim e^{-d/27.9}$. **b** Distribution of travel duration $\tau$, with most trips lasting around 38 minutes. **c** Distribution of dwell time at stays $\delta$, capturing that residents tend to remain at home for around 560 minutes.

To infer home locations, we analyze the refined stays by examining both their temporal patterns and visit frequencies. We focus on locations visited most frequently during nighttime hours (i.e., 21:00 to 6:00) across multiple days. The location with the highest cumulative duration during these nighttime periods is designated as the likely home location for an individual, provided that it meets a minimum threshold of 25 visits over the 30-day observation period. Additionally, we validate these candidates by comparing weekend visit durations, under the assumption that true home locations typically exhibit higher activity during weekends. Amap residential POIs are leveraged to ensure that the identified candidate is situated within a residential area. If multiple locations meet these criteria, the candidate with the longest total nighttime duration is selected as the home location. For workplace detection, we apply a similar approach by focusing on significant stays during typical working hours (i.e., 9:00 to 17:00) on workdays. We identify locations that exhibit both high frequency and long cumulative durations of stays during these hours, setting a threshold of at least 4 visits per 5 workdays to qualify as potential workplace candidates. Amap commercial POIs are used to validate these candidates, ensuring that the identified location is consistent with common workplace settings. Among the candidates, the location with the longest total working-hour duration is selected as the workplace for each individual. We successfully infer home locations and workplaces of 6.05 million individuals, ensuring that only users with robust and consistent activity patterns are included in the final dataset. Unidentified users, for whom home or workplace cannot be reliably determined, are excluded to maintain the accuracy and reliability of our analysis.

Distributions of home locations and workplaces of individuals (Supplementary Fig. 2) suggest that both residential and employment densities are higher in the city center, while commuting flows tend to be more localized within nearby neighborhoods. Daily movements between homes and workplaces show predictable time patterns. People's time spent at home and workplaces follows opposite daily rhythms—home presence typically peaks overnight particularly on weekends, whereas workplace presence peaks during daytime hours and on workdays (Supplementary Fig. 3).

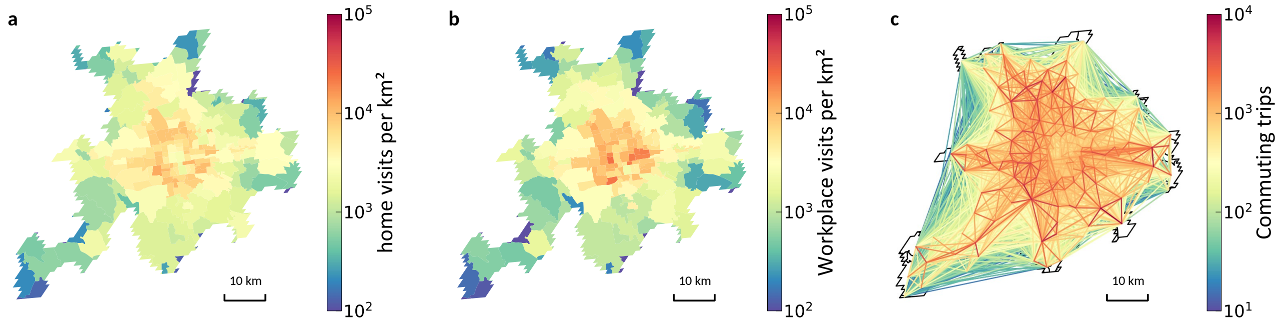


**Supplementary Figure 2 | Jobs-housing structure of Beijing metropolitan area. a** Spatial clusters of home locations. Individuals' home-based trips are aggregated to township administrative boundaries, and the mobility counts are normalized by jurisdictional area (km²). **b** Spatial clusters of workplaces. **c** Spatial distribution of commuting flows.

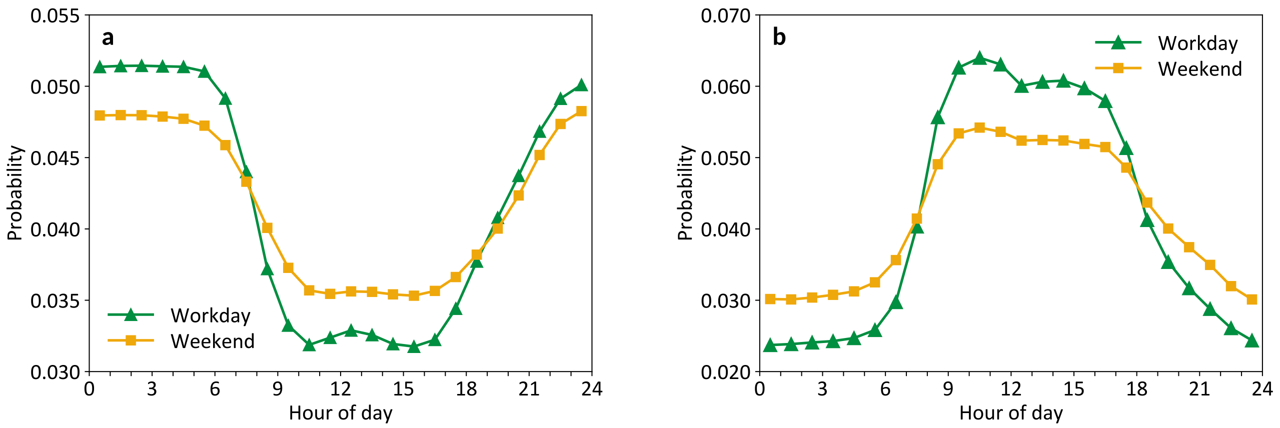


**Supplementary Figure 3 | Daily patterns of time spent at homes and workplaces. a** Home presence probabilities across hours of day. **b** Workplace presence probabilities across hours of day.

## 1.2 Population representativeness

We validate the population representativeness of mobile phone data through cross-validation with China's Seventh National Population Census [2]. This nationwide census, conducted by the National Bureau of Statistics (NBS), provides comprehensive demographic data across 41,636 township-level administrative units encompassing all 31 provincial divisions. To address temporal discrepancies between the decennial census (2020) and our mobility dataset (2023), we incorporate annual population growth estimates (0.87% average increase) derived from Beijing Municipal Statistical Yearbooks (2020-2023) [3–6]. The population distribution in Beijing's metropolitan region is visually summarized in Supplementary Fig. 4a. Our validation strategy involves examining the correlation between census-recorded resident populations and home-based trip frequencies derived from mobility data at matched township units. This approach is grounded on the inherent stability of residential behavior [7], hypothesizing that home-based trip frequencies constitute reliable proxies for static population distributions. Across all township units, we compute Pearson's correlation coefficient ($r$) between the two datasets.

A robust coefficient of $r = 0.8426$ (***$p < 0.001$; 95% CI [0.7943, 0.8804]) indicates a statistically significant positive association, explaining 71.0% of shared variance ($r^2 = 0.710$) (Supplementary Fig. 4b). This strong correspondence confirms the capacity of mobile phone data to reliably approximate population distribution patterns at fine spatial scales.

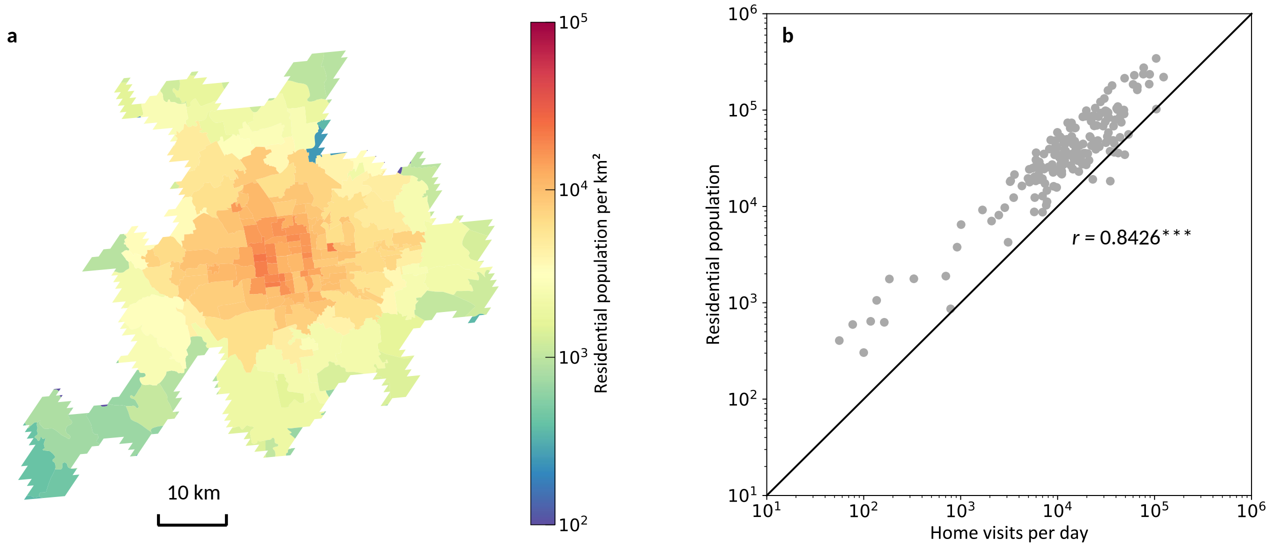


**Supplementary Figure 4 | Population representativeness validation. a** Census population distribution in Beijing metropolitan region. **b** Scatter plot illustrating correlation between census population and home-based trip frequency indicated by Pearson's correlation coefficient $r$, with the diagonal line providing the reference. Point represents a township-level administrative unit. *** indicates statistical significance $p < 0.001$.

## 1.3 Socioeconomic status inference

To infer the income levels of individuals, we establish a connection between the individuals' inferred home locations and the LianJia property database—China's largest real-time property transaction platform covering 97.3% of residential markets. This database provides detailed, geotagged records of residential communities, including information such as community name, average transaction price (in RMB per square meter), architectural type (high-rise towers, slab complexes, bungalows), number of households and buildings in the community, and exact location (precise latitude and longitude coordinates). It is important to note that housing in China is typically organized into well-defined residential communities. Unlike many Western settings where neighborhoods might comprise a mix of varied housing styles and unplanned developments, these communities are generally gated, uniformly managed, and offer shared amenities such as green spaces and retail facilities. This structured arrangement not only standardizes property types within a community but also results in more homogenous pricing and quality measures across the board. Therefore, platforms like LianJia can efficiently capture a near-complete snapshot of the housing market, thereby serving as a reliable proxy for inferring the socioeconomic status of residents based on their home locations.

In the Beijing metropolitan area, the database lists 9,501 communities with price data as of June 2023, as illustrated in Supplementary Fig. 5a. We perform a spatial query to match the individual's home coordinates (latitude and longitude) with communities listed in the LianJia database. Specifically, we construct Voronoi polygon around each community, creating non-overlapping zones where all points within a polygon are geographically closer to its central community than to others (Supplementary Fig. 5b). These Voronoi polygons effectively capture localized market conditions, as residents within the same polygon are likely to experience similar socioeconomic environments. For every individual, we identify the polygon containing the inferred home location and assign the associated community transaction price as an approximate measure of that individual's income level. To ensure reliability, we compute the geographic distance between each individual's home and the matched community. Our analysis reveals that 80% of home locations are within 250 meters of a community, and 90% are within 500 meters (Supplementary Fig. 5c). These findings confirm that the majority of individuals reside in close proximity to the communities used in our analysis, thereby demonstrating the robustness of income inference.

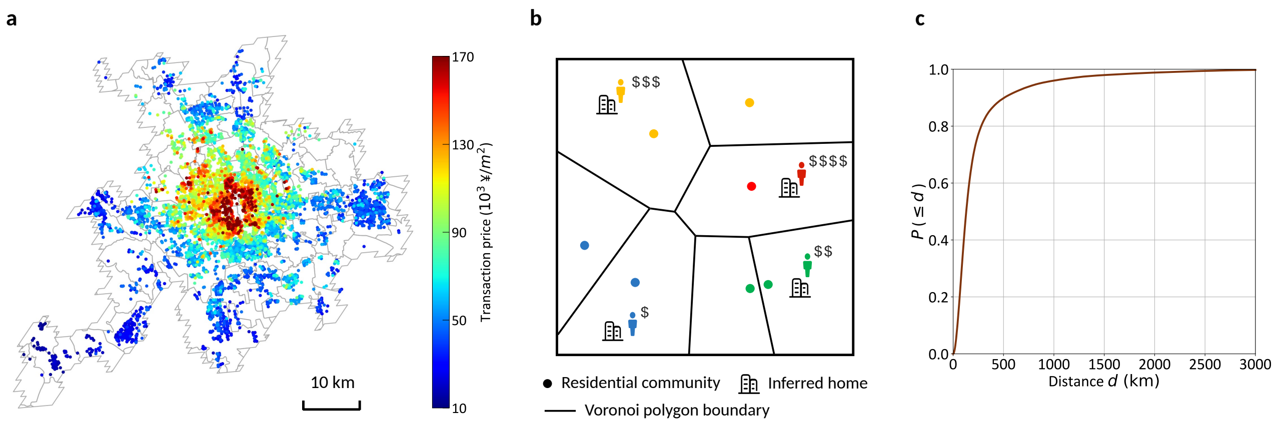


**Supplementary Figure 5 | Spatial matching analysis based on LianJia property data.** **a** Geospatial visualization of 9,501 communities listed on the LianJia platform, with color coding indicating average transaction prices as of June 2023. **b** Construction of Voronoi polygons around each community. Individual's home location within a polygon is assigned the transaction price of the corresponding community, establishing localized socioeconomic proxies. **c** Distance distribution between residences and matched communities.

Individuals are divided into four equal groups based on the 25th, 50th, and 75th percentiles of the inferred income levels derived from the matched community transaction prices. Each quartile corresponds to a distinct income group. For instance, the first quartile, which contains individuals with property transaction prices at or below the 25th percentile, is assumed to represent the lower-income group. The second quartile (between the 25th and 50th percentiles) represents the lower-middle-income group, the third quartile (between the 50th and 75th percentiles) represents the upper-middle-income group, and the fourth quartile (above the 75th percentile) represents the higher-income group. The spatial distributions of home and workplace locations for these four income groups are shown in Supplementary Fig. 6.

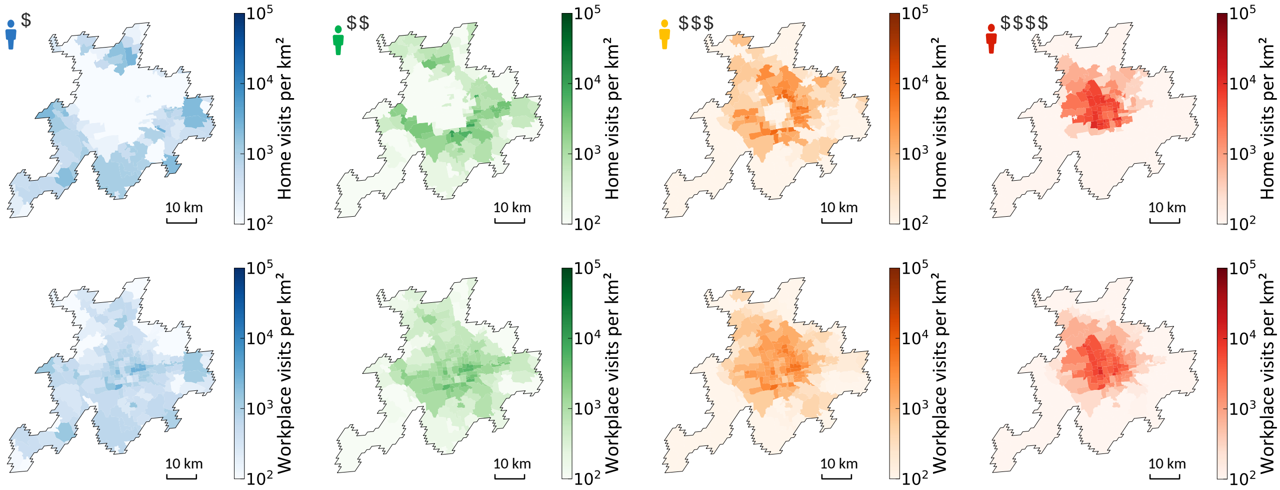


**Supplementary Figure 6 | Spatial distributions of residential locations and workplaces for four income groups.** Top row: Residential distributions reveal strong income stratification, with higher-income groups concentrated within city core area, transitioning to lower-income groups in peripheral districts. Bottom row: Workplace distributions display more evenly spatial patterns, maintaining partial concentration in central business districts across all income groups.

## 1.4 Travel mode choices

For each individual trip, we compute the probabilities that an individual travels through particular transport mode (active, private or public) using a pre-trained random forest model calibrated on the publicly available Geolife dataset [8]. The Geolife dataset, collected by Microsoft Research Asia, comprises GPS trajectories of over 180 users in a range of cities, primarily in Beijing, China, over several years. We segment each trajectory into multiple contiguous trips, defined by a minimum dwell time of 15 minutes between trips. Each trip is labeled with ground-truth transport modes (one or more) used, including walking, cycling, car, taxi, bus, railway. We consolidate similar modes (e.g., walking and cycling into "active"; car and taxi into "private"; bus, railway into "public") to align with our defined categories. Trips involving a combination of private and public modes are excluded from the analysis to ensure unambiguous mode classification. Only trips exclusively involving active modes are labeled as "active"; all other trips are categorized as either "private" or "private" based on their dominant mode. In Beijing metropolitan area, this process yields 1,819 active trips, 881 private trips, and 1,725 public trips.

To train the random forest model, we extract five features relevant to transport mode identification, including: 'Route length' (total distance traveled during the trip), 'OD distance' (Euclidean distance between origin and destination), 'O_pubstation_dist' (distance from the origin to the nearest public transportation station obtained from Amap POIs), 'D_pubstation_dist' (distance from the destination to the nearest public transportation station), and 'Travel time' (duration of the trip). The model is trained using a subset of the Geolife data (80% for training, 20% for validation) and optimized for classification accuracy. To mitigate potential sample imbalance, the model is configured to automatically adjust the weights assigned to each class based on their prevalence in the data, ensuring that classes with fewer samples are given more importance during training. The contribution of each feature to the model's predictions is shown in Supplementary Fig. 7. Rather than assigning a single, definitive mode for each trip, the model generates probabilistic mode assignments, reflecting pre-trip decision uncertainty. For instance, a particular trip might be assigned probabilities of 0.1 for "active", 0.6 for "private", and 0.3 for "public". This suggests that while private mode is the most probable, there's still a non-negligible chance of choosing public transport. Such probability vectors capture travelers' latent preference influenced by contextual factors prior to a trip.

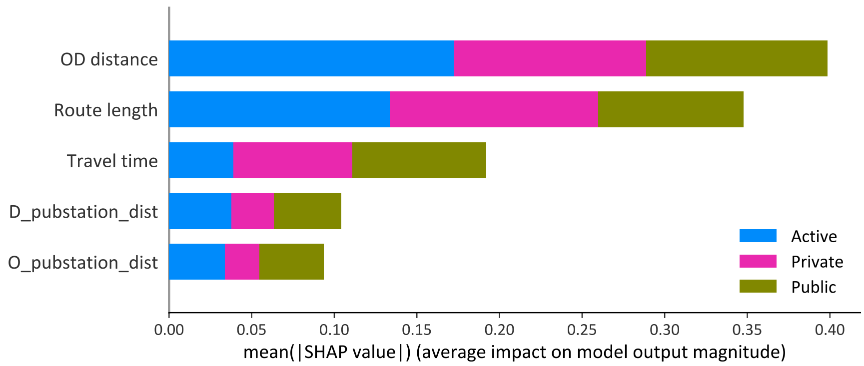


**Supplementary Figure 7 | Overall feature importance based on SHAP (SHapley Additive exPlanations) values for the travel mode inference model.** Features are listed on the vertical axis, ordered from most to least important. The horizontal axis represents the mean absolute SHAP value for each feature. A longer bar indicates a greater overall impact of that feature on the model's predictions across the entire dataset.

The model's performance is evaluated through metrics appropriate for both classification and probability estimation. Specifically, Receiver Operating Characteristic (ROC) curves [9] (Supplementary Fig. 8a), which assess the model's ability to discriminate between classes, yield high Area Under the Curve (AUC) scores: 0.9575 for active mode, 0.9242 for private mode, and 0.9213 for public mode, indicating strong discriminatory capacity across all modes. Furthermore, the calibration of the probability estimates is assessed using the Brier score [10], which measures the mean squared difference between predicted probabilities and actual outcomes. The Brier scores are also favorable (Supplementary Fig. 8b): 0.073 for active mode, 0.076 for private mode, and 0.109 for public mode, demonstrating well-calibrated probability predictions.

This pre-trained random forest model is then applied to our mobile phone dataset. For each trip in this dataset, we calculate the same five features: 'Route length', 'OD distance', 'O_pubstation_dist', 'D_pubstation_dist', and 'Travel time'. By inputting these features into the trained model, we estimate the probability distribution across active, private, and public transport modes for each trip. These probability estimates are then used for further mobility analysis.

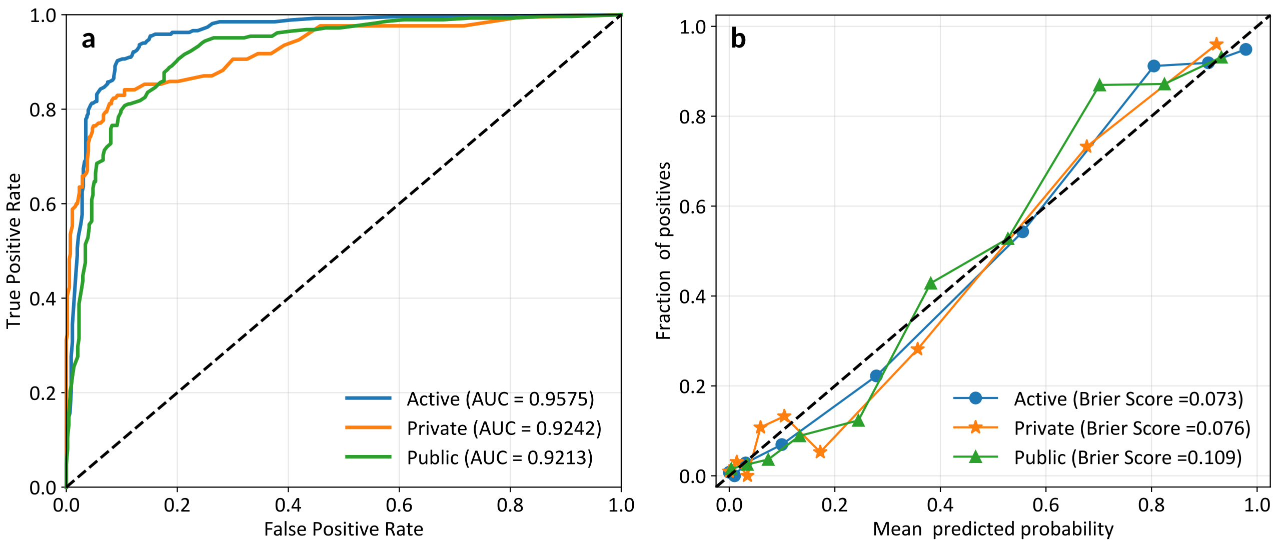


**Supplementary Figure 8 | Model performance evaluation. a** Receiver Operating Characteristic (ROC) curves. Each curve plots the True Positive Rate against the False Positive Rate at various threshold settings. The Area Under the Curve (AUC) for each mode is indicated in the legend. High AUC values (close to 1) demonstrate the model's excellent ability to distinguish between each transport mode and the others. **b** Calibration curves assess the reliability of the predicted probabilities by plotting the observed fraction of positives against the predicted probabilities. Ideally, the calibration curves should closely follow the diagonal (dashed line), indicating well-calibrated probabilities where predicted probabilities align with actual event frequencies. Lower Brier scores (close to 0) indicate better calibration.

## 1.5 Travel route generation

For each trip of an individual, we generate a most probable travel route for active, private, and public modes respectively using Amap navigation API [11], a sophisticated service renowned for its routing capabilities in China. The Amap API is configured to generate routes by considering a range of input parameters including the trip origin and destination coordinates (latitude and longitude), waypoints, departure time and desired travel modes. Critically, the API computes the most time-efficient route for the specified mode, dynamically factoring in real-time traffic conditions, public transit schedules, estimated costs, and general traveler preferences as modeled within its algorithms. To enhance the realism of these generated routes, we incorporate all GPS trajectory points from each original trip record as intermediate waypoints when querying the API. This strategy allows the navigation system to compute routes that more accurately capture potential deviations, detours, and individual preferences that may have influenced the observed travel behavior. The resulting output from the Amap API delivers comprehensive navigation information. For active and private modes, this includes a breakdown of route details by road segment, specifying the roads to be taken and the estimated travel duration for each segment, accounting for real-time traffic where applicable. For public mode routes, the API details the specific transit lines to utilize, the sequence of stations, the estimated travel time between stations, and any necessary transfer points. The use of Amap API allows for privacy-preserving travel planning by inferring potential routes without directly accessing sensitive location data from the individual's mobile device.

To validate the accuracy of route generation process, we leverage the high-resolution GPS trajectories provided in the Geolife dataset as ground truth. Notably, the majority of these trajectories (91.5%) are recorded at a dense sampling rate, typically every 1–5 seconds, ensuring a detailed and accurate representation of travel paths. For each trip, we generate a route between its origin and destination using the Amap API corresponding to the actual travel mode recorded in Geolife data. To quantitatively assess the spatial similarity between the generated route and the actual GPS trajectory, we create a buffer around both the generated route $B_{generated}$ and the original GPS trajectory $B_{real}$, and calculate the Jaccard index, representing the ratio of the intersection area to the union area of the two buffers

$$J = \frac{Area(B_{generated} \cap B_{real})}{Area(B_{generated} \cup B_{real})} \tag{S1}$$

This index provides a measure of overlap, with higher values (close to 1) indicating greater agreement between the generated route and the real-world trajectory. For 4,425 mode-labeled trips in Geolife dataset, we test a range of buffer distances—30 meters, 50 meters, 70 meters, and 90 meters—around both the Amap-generated routes and the corresponding real GPS trajectories. We observe that even under a stringent 30-meter buffer, over 70% of generated routes achieve a Jaccard index greater than 0.5 (Supplementary Fig. 9). This threshold of 0.5 signifies a substantial level of overlap, suggesting that the generated routes closely align with the real-world trajectories in a majority of cases. When examining the results across different modes, we observe no significant differences in performance. This validation demonstrates the Amap API's effectiveness in generating realistic routes.

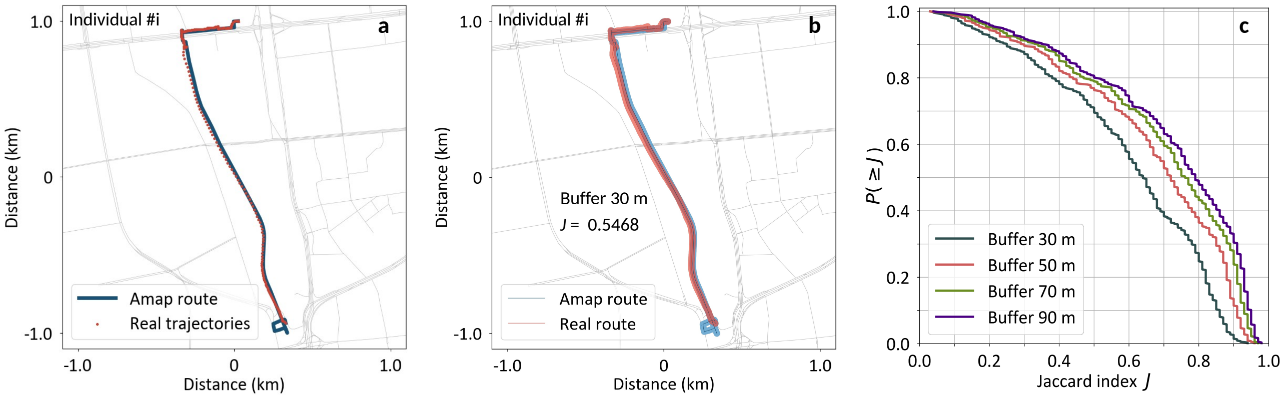


**Supplementary Figure 9 | Validation of Amap route generation against Geolife GPS trajectories. a** An example of an Amap-generated route overlaid with the corresponding real GPS trajectory from Geolife for a single trip. **b** Buffered representation (30-meter buffer) of the generated and real routes. **c** Cumulative distribution of Jaccard Index $J$ across 4,425 mode-labeled trips from the Geolife dataset, shown for different buffer distances (30m, 50m, 70m, and 90m).

## 1.6 Cross-data validation

To further validate the reliability of travel mode inference and route generation processes, we leverage an additional independent dataset to compare the consistency of mobility flow distributions in urban spaces. We use the open-sourced MemDA data [12], which comprise traffic speeds from major roads in Beijing collected in a period of 75 days (from May 12, 2022, to July 25, 2022). In urban road traffic, the average speed of a road segment is typically negatively correlated with traffic volume under most normal conditions, as higher vehicle densities tend to reduce speeds due to congestion. We process the traffic speed data by aggregating measurements into hourly intervals for each major road segment over the 75-day period. The average speed per segment per hour is computed as the mean of all recorded speeds within that time window, providing a proxy for potential traffic condition. For the mobile phone dataset, we calculate the expected traffic volume for each road segment in a given hourly interval by summing the estimated private mode probabilities of all trips whose Amap-generated routes include that segment during that time period. For example, a trip with a 0.7 probability of private mode contributes 0.7 vehicle units to the traffic volume of each segment along its route. This probabilistic aggregation reflects the uncertainty in mode choice predictions and provides a robust estimate of traffic flow. To compare the two datasets, we normalize the MemDA-derived average speeds and the mobile phone-derived expected traffic volumes for matching road segments and hourly intervals. The spatial distributions of these normalized values during the morning peak hour (9:00-10:00) is visualized in Supplementary Fig. 10, revealing a notable spatial consistency, which is supported by a significant negative Pearson correlation coefficient of $r$ = -0.3191 ($p < 0.001$; 95% CI [-0.3504, -0.2871]) (Supplementary Fig. 11a). We also observe similarly significant negative correlations during the midday (13:00-14:00, $r$ = -0.3521; 95% CI [-0.3826, -0.3209]) and evening peak (17:00-18:00, $r$ = -0.3513; 95% CI [-0.3819, -0.3201]) hours (Supplementary Fig. 11bc). This temporal and spatial consistency across the MemDA and mobile phone datasets underscores the method reliability in capturing road traffic patterns.

# 2 Measuring encounter opportunities in interconnected urban spaces

We develop two measures to quantify the opportunities for social encounters created by multimodal mobility at the city scale. The first one is the mode-specific Probabilistic Mixing Index (PMI), which is designed to capture the diversity of potential encounters experienced by individuals when using a particular transport mode. The second one is the Multimodal Uniformity Index (MUI), which builds upon the PMI to assess the consistency of these encounter opportunities across different travel modes within a geographical region.

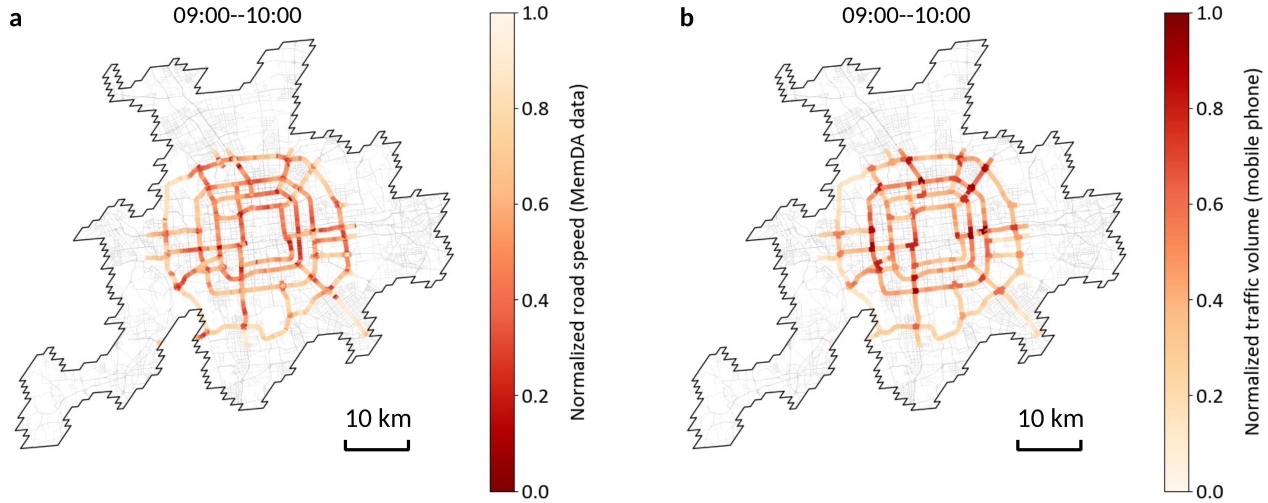


**Supplementary Figure 10 | Spatial consistency of mobility flow distributions across datasets in Beijing metropolitan area. a**, Spatial distribution of normalized road average speed from MemDA data during the morning peak hour (9:00-10:00). **b**, Spatial distribution of normalized expected road traffic volumes inferred from mobile phone data for private mode during the morning peak hour.

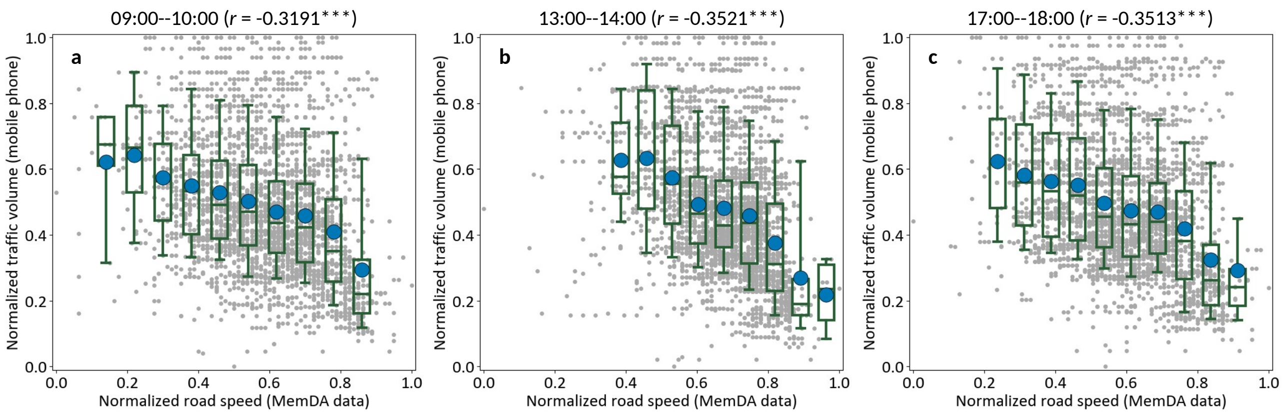


**Supplementary Figure 11 | Cross-data validation performance.** Correlation between normalized average traffic speeds from MemDA data and normalized expected traffic volumes inferred from mobile phone data for private modes during the morning peak (9:00-10:00; panel **a**), midday (13:00-14:00; panel **b**) and evening peak (17:00-18:00; panel **c**) hours. Pearson correlation coefficient of $r$ is marked on the title, with *** indicating statistical significance $p < 0.001$. In all panels, grey points represent road segments, plotted according to their values from the two datasets being compared. Boxplots are grouped by bins of values from the reference dataset on the x-axis, and show the distribution of the corresponding values from mobile phone data on the y-axis within each bin. Blue points represent the average value within each bin, summarizing the overall trend.

## 2.1 Probabilistic Mixing Index

The mode-specific Probabilistic Mixing Index (PMI) is calculated based on the probabilities of individuals' paths overlapping in multilayered urban spaces while traveling via a specific mode. After data fusion processing, we have estimated the probabilities that an individual travels through different transport modes (active, private, or public) (Supplementary Section 1.4), and generated a most probable travel route corresponding to each mode (Supplementary Section 1.5). For road transportation (active and private), the generated route specifies the road segments to be taken and the estimated duration. For public transportation (bus and railway), the generated route provides the station-by-station trajectories within transit systems, including the specific sequence of stations, along with the estimated travel times between them. For a given departure time, the geographical location at any moment along the route of a specific mode can be determined, as shown in Supplementary Fig. 12a.

For simplicity, we assume that encounter opportunities arise from transient co-presence in time and space with others traveling via the same mode. These co-locations represent moments when two or more individuals are present in the same spatial unit simultaneously while using the same mode. To capture these potential encounters, the urban space is partitioned into mode-specific spatial units, reflecting the distinct ways individuals perceive and interact with their surroundings. The spatial scales for active and private modes are defined as 1 km × 1 km grids. For active (or private) mode, two individuals' routes are mapped onto the 1 km × 1 km grids over time. A co-location occurs when they occupy the same grid within a specific time frame, indicating a potential encounter. For bus and railway modes, the spatial units are the transit segments between stations. In this context, co-locations occur within the confined spaces of transit vehicles or at stations, capturing the shared experience inherent to public transit. These spatial units are analyzed within 1-hour time frames, a temporal resolution chosen to balance computational feasibility with the need to capture significant social interactions.

To calculate the PMI for each spatial unit, mode, and 1-hour time frame, the expected number of individuals from each income group is computed by summing the product of their mode-choice probability and an indicator of their presence in that spatial unit. Mathematically, for a spatial unit $s$, time frame $t$, and income group $q$, the expected population can be expressed as:

$$E_{s,t,q} = \sum_{i \in q} p_{i,m} \cdot I_{i,s,t} \tag{S2}$$

where $p_{i,m}$ is the probability that individual $i$ travels via mode $m$, and $I_{i,s,t}$ is an indicator variable equal to 1 if individual $i$'s route using mode $m$ passes through spatial unit $s$ during time frame $t$, and 0 otherwise. Each individual contributes a fractional value—reflecting their partial likelihood of being present—to the expected population. This expected value accounts for the inherent uncertainty in individual travel behavior, providing a more dynamic and realistic estimate of population distribution. For example, if an individual from group $q$ has a 0.9 probability of choosing to drive and their driving route passes through spatial unit $s$ between 8 and 9 AM, their contribution to $E_{s,t,q}$ for driving would be $0.9 \times 1 = 0.9$. A schematic illustration of the calculations is shown in Supplementary Fig. 12bc. After computing the expected population $E_{s,t,q}$ for each of the four income groups, the PMI is derived using an entropy metric to quantify the diversity of the potential encounters, calculated as:

$$PMI_{s,t,m} = -\frac{1}{\log(4)} \sum_{q=1}^{4} \tau_{s,t,q} \cdot \log(\tau_{s,t,q}) \tag{S3}$$

where $\tau_{s,t,q} = \frac{E_{s,t,q}}{\sum_{q=1}^{4} E_{s,t,q}}$ denotes the proportion of the total expected population in spatial unit $s$, time frame $t$, and mode $m$ that belongs to income group $q$. The normalization factor $\frac{1}{\log(4)}$ scales the entropy to a range between 0 and 1. A $PMI_{s,t,m}$ value of 0 indicates minimal mixing potential (i.e., only one income group is present), while a value of 1 indicates maximum mixing potential (i.e., all four income groups are equally represented).

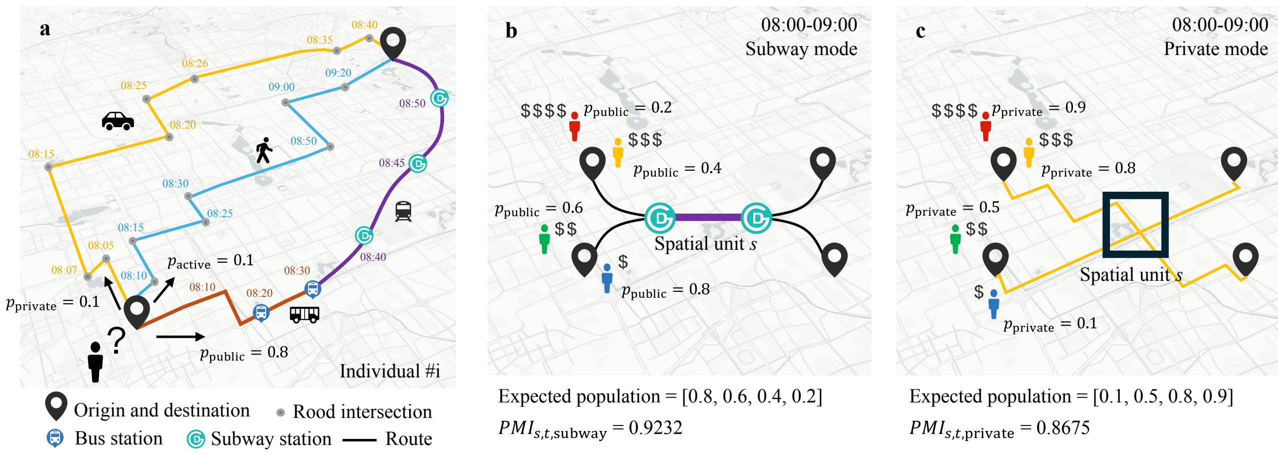


**Supplementary Figure 12 | Illustration of the calculation of the Probabilistic Mixing Index (PMI). a** Individual mode choice probabilities and time-stamped paths for active, private, and public modes. **b** Example of PMI calculation for a single spatial unit (transit segment) for a railway line. Assuming four individuals from four income groups are co-located at this segment between 8–9 AM, their contributions to the expected population $E_{s,t,q}$ equal their mode choice probabilities. **c** Example of PMI calculation for a single spatial unit (1 km × 1 km grid) for individuals driving.

## 2.2 Multimodal Uniformity Index

The Multimodal Uniformity Index (MUI) is introduced to evaluate how consistently encounter opportunities are distributed across different travel modes within the same geographical region. For a specific region $A$ and time frame $t$, we first calculate the average mixing level $PMI_{A,t,m}$ for a given mode $m$ across all relevant spatial units $s$ in region $A$ during period $t$:

$$PMI_{A,t,m} = \frac{1}{|S_A|} \sum_{s \in S_A} PMI_{s,t,m} \tag{S4}$$

where $S_A$ is the set of spatial units (grids for active and private modes, transit segments for bus and railway modes) associated with region $A$, and $|S_A|$ is the number of such units. The spatial units in $S_A$ are defined based on the characteristics of each travel mode. For active and private modes, a spatial unit $s$ (1 km $\times$ 1 km grid) is included in $S_A$ if any portion of it overlaps with the region. For public transportation, a spatial unit (transit segment) is included in $S_A$ if at least one of its endpoint stations is located within this region, reflecting the service provision within the defined geographical area (Supplementary Fig. 13). With $PMI_{A,t,m}$ computed for each mode—active, private, bus, and railway—we then normalize these values into proportions $r_{A,t,m} = PMI_{A,t,m}/\sum_m PMI_{A,t,m}$, where the sum is taken over the four modes. The MUI for region $A$ at time $t$, denoted $MUI_{A,t}$, is then calculated using the entropy formula:

$$MUI_{A,t} = -\frac{1}{\log(4)} \sum_m r_{A,t,m} \log(r_{A,t,m}), \tag{S5}$$

An $MUI_{A,t}$ value close to 1 indicates high uniformity, meaning mixing opportunities are similar across all modes in region $A$. A value near 0 suggests that encounter opportunities are highly stratified by mode choice, with significant variation in mixing levels between modes. This index thus provides a time-specific measure of how equitably transportation modes contribute to social encounter patterns within a region.

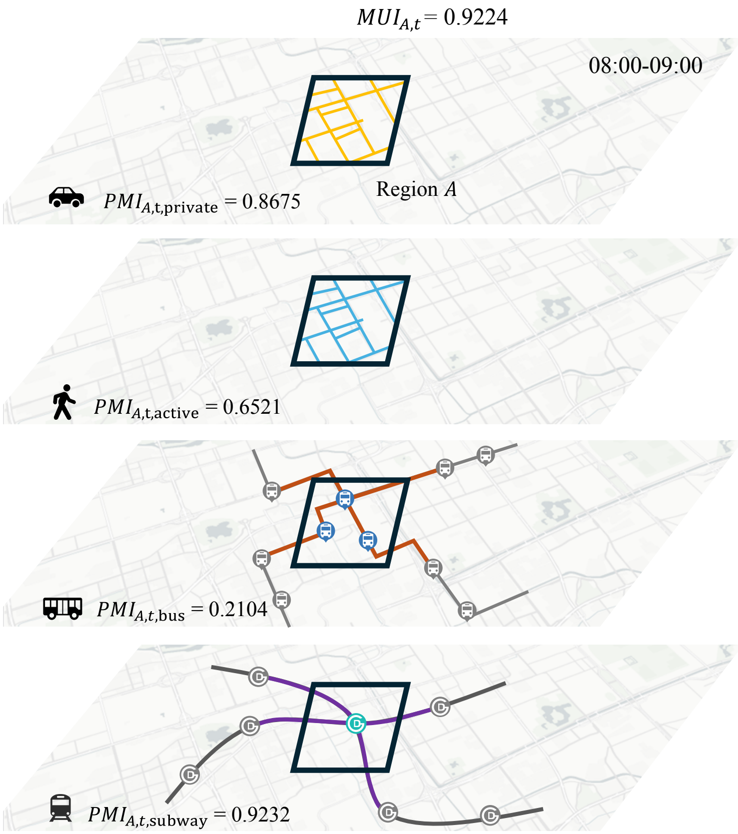


**Supplementary Figure 13 | Illustration of the calculation of the Multimodal Uniformity Index (MUI).** The region-level mixing potential $PMI_{A,t,m}$ for each mode $m$ is first calculated by aggregating all relevant spatial units in region $A$. $MUI_{A,t}$ is then computed by normalizing these $PMI_{A,t,m}$ values into proportions and applying the entropy formula, indicating the uniformity of encounter opportunities across modes in region $A$ during time $t$.

## 2.3 Sensitivity analysis of spatiotemporal scales

In this study, the primary results are presented using spatiotemporal scales that balance computational efficiency with the ability to capture meaningful social interactions, specifically a temporal resolution of 1 hour and spatial scales of 1 km $\times$ 1 km grids for active and private modes, and transit segments for public transportation modes. To evaluate the robustness of the Probabilistic Mixing Index (PMI) and the Multimodal Uniformity Index (MUI) to variations in these scales, we conduct a sensitivity analysis by systematically testing alternative temporal and spatial resolutions.

For temporal scales, we examine window sizes ranging from 3 to 60 minutes. For spatial scales, we test grid resolutions from 250 m to 2 km for active and private modes, while keeping the transit segment definition unchanged for public transportation.

Figure 14 presents the cumulative distributions of PMI for each of the four travel modes across the range of temporal scales. As the temporal scale increases, the cumulative distribution curves generally shift upwards, indicating a tendency towards higher PMI (greater mixing potential) with longer periods. This effect is most pronounced for the bus mode, as evidenced by the Kolmogorov-Smirnov (K-S) statistic [13] comparing 3-minute and 60-minute windows: bus mode exhibits the largest distributional divergence (K-S = 0.3566, $p < 0.001$), followed by private (K-S = 0.1874), railway (K-S = 0.1825), and active modes (K-S = 0.1257; all $p < 0.001$). The heightened sensitivity of bus systems likely stems from their variable ridership patterns and frequent stops, which amplify transient co-location noise in short time frames.

Figure 15 presents spatial scale sensitivity by comparing cumulative PMI distributions for active and private modes across grid resolutions from 250 m to 2 km. Larger spatial scales produce upward-shifted distribution curves, reflecting higher PMI values at coarser resolutions. The K-S statistic quantifies this divergence, with private modes exhibiting greater sensitivity (K-S = 0.1976, $p < 0.001$) compared to active modes (K-S = 0.1560, $p < 0.001$). The relatively low magnitude of the K-S statistics suggests that PMI distributions for both modes remain reasonably stable across the tested range of spatial scales.

Figure 16 presents the sensitivity of the Multimodal Uniformity Index (MUI) to spatiotemporal variations. In Supplementary Fig. 16a, comparing temporal scales from 3 to 60 minutes yields a K-S statistic of 0.4329 ($p < 0.001$), indicating a notable shift in uniformity. In Supplementary Fig. 16b, varying the spatial scale from 250 m to 2 km yields a much larger K-S statistic of 0.7580 ($p < 0.001$). A key observation is the presence of two significant phase transitions in the MUI distribution, at approximately 0.5 and 0.8. These transitions correspond to distinct grid characteristics related to transit availability. The phase transition at $MUI \approx 0.5$ captures grids that lack both bus and railway stations, leaving only two modes (active and private) contributing to the MUI calculation (approximating $\frac{\log(2)}{\log(4)} = 0.5$). The second transition at $MUI \approx 0.8$ corresponds to grids without railway stations but with bus stations, meaning three modes contribute (approximating $\frac{\log(3)}{\log(4)} \approx 0.7925$). These transitions reflect discrete drops in the number of available travel modes, which directly impacts the uniformity of encounter opportunities.

Despite the influence of scale on the metric distributions, universal patterns are captured across different spatial resolutions (Supplementary Fig. 17). Specifically, the spatial distributions of PMI and MUI in the Beijing metropolitan area reveal consistent trends, such as lower mixing potential in peripheral regions and greater uniformity in central urban cores, regardless of whether the grid size is 250 m or 2 km. These findings suggest that while the absolute values of the metrics may shift with scale, the underlying spatial organization of encounter opportunities exhibits robust, scale-invariant characteristics.

# 3 OLS models explaining spatiotemporal patterns of encounter opportunities

We use ordinary least squares (OLS) regression models to explain how transport infrastructure influences the patterns of encounter opportunities observed through the Probabilistic Mixing Index (PMI) and the Multimodal Uniformity Index (MUI). The form of the OLS regression model is:

$$M_t = \beta_0 + \sum_i \beta_{T_i} T_i + \epsilon_t, \tag{S6}$$

where:

- $M_t$ is the dependent variable, representing either the observed regional-level mixing index ($PMI_{A,t,m}$, Eq. S4) for a specific travel mode $m$ (active/private/bus/railway) or the $MUI_{A,t}$ (Eq. S5) across four modes within region $A$ at a specific period $t$. The analysis is conducted at a spatial scale of 1 km $\times$ 1 km grids, which define the regions $A$.

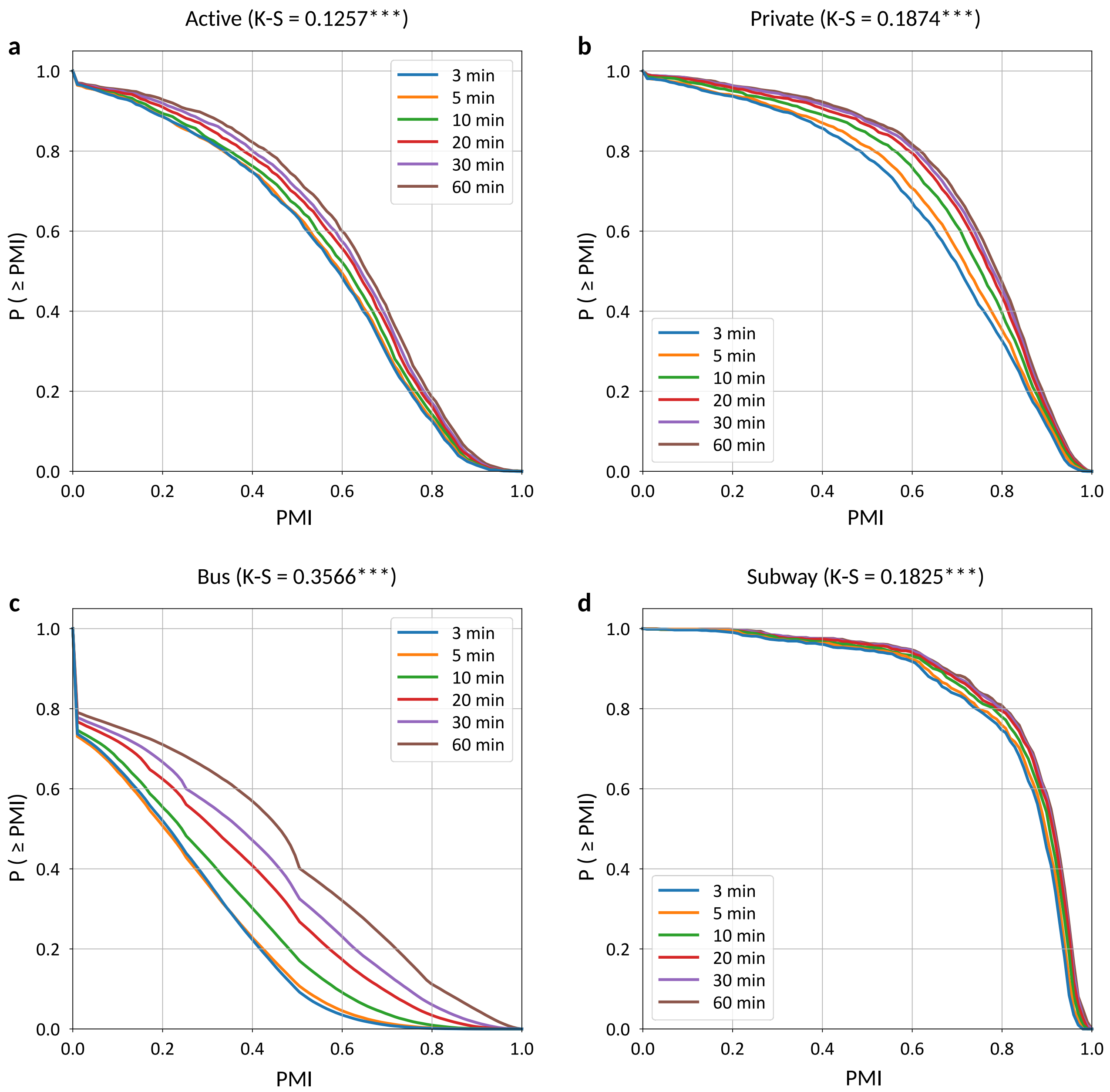


**Supplementary Figure 14 | Cumulative distributions of PMI for four travel modes across different temporal scales under fixed 1 km × 1 km grids.** The Kolmogorov-Smirnov (K-S) statistics (*** indicates p-value $< 0.001$) quantify the distributional divergence between the 3-minute and 60-minute temporal scales.

- $\{T_i\}$ denotes the set of transport infrastructure-related explanatory variables. These include lengths of different road types (Motorway, Primary, Secondary, Tertiary, Pedestrian roads), road diversity (calculated using the entropy of road types within a grid), and counts of transport facilities (e.g., Bus Stations, Subway Stations), reflecting the transportation and built environment features of the grids. Grid-level statistics for these variables are detailed in Supplementary Table 1.
- $\beta_0$ is the intercept of the regression model.
- $\beta_{T_i}$ are the regression coefficients corresponding to the transport infrastructure variables, quantifying their individual contributions to $M_t$.
- $\epsilon_t$ is the error term, capturing unexplained variation in the model.

To capture temporal heterogeneity in the dynamics of encounter opportunities, we design two model variants with distinct temporal granularity. **(1) Daily granularity model:** Separate models are estimated for workdays and weekends. For a specific day type $d$, the dependent variable $M_t$ for each grid $A$ is calculated as the average

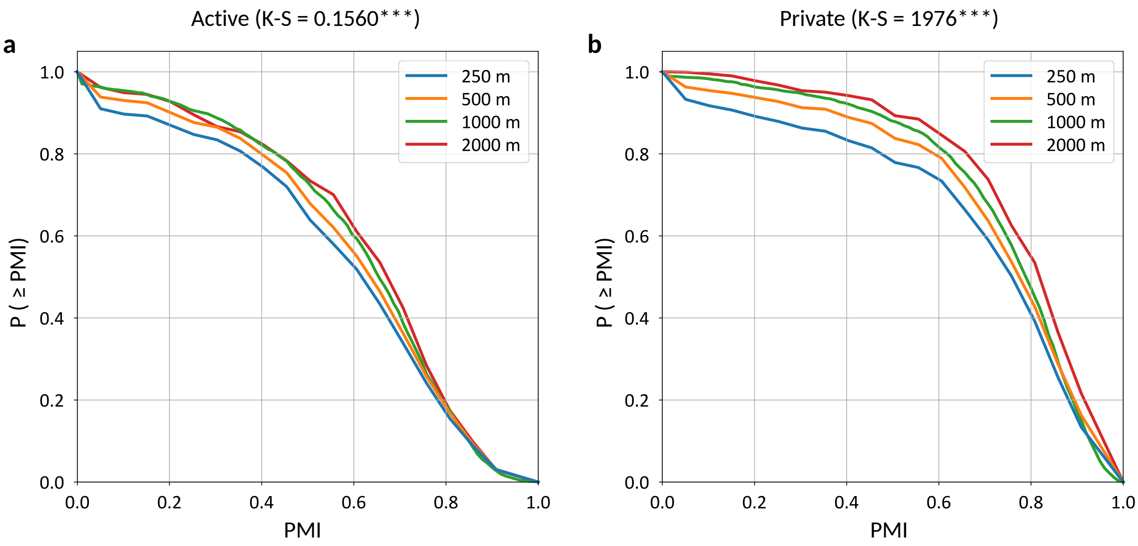


**Supplementary Figure 15 | Cumulative distributions of PMI for active (panel a) and private (panel b) modes across spatial scales under a fixed 60-minute temporal scale.** The Kolmogorov-Smirnov (K-S) statistics (*** indicates p-value $< 0.001$) quantify the distributional divergence between the 250 m and 2 km grid scales.

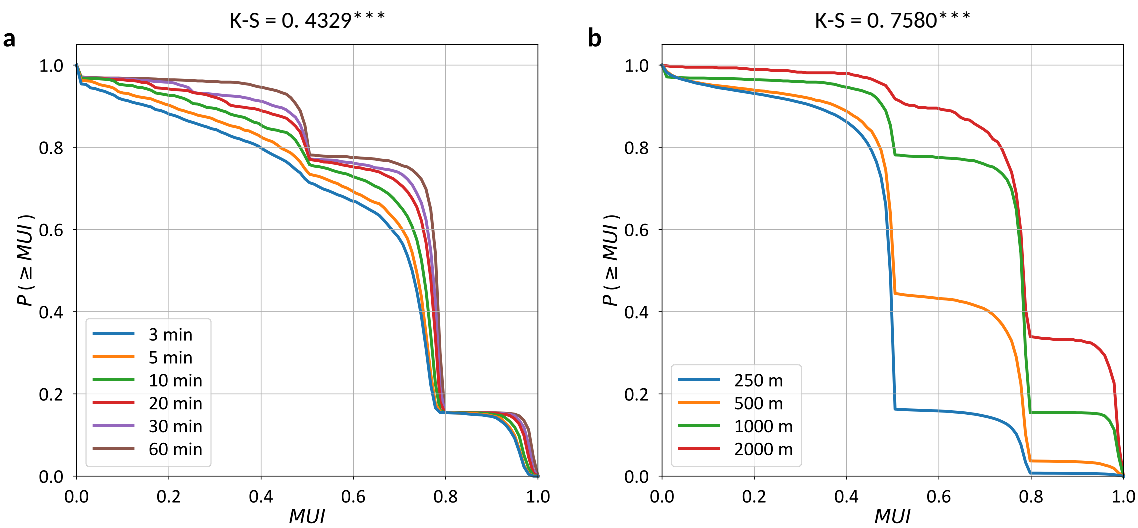


**Supplementary Figure 16 | Cumulative distributions of MUI for urban grids across different spatiotemporal scales. a** Temporal sensitivity analysis. **b** Spatial sensitivity analysis. The Kolmogorov-Smirnov (K-S) statistic (*** indicates p-value $< 0.001$) quantifies the distributional divergence between the minimum and maximum scales tested in each panel.

value of the mixing index ($PMI_{A,t',m}$ or $MUI_{A,t'}$) across all hourly periods $t'$ within that day. **(2) Hourly granularity model:** Separate models are estimated for each specific hour of the day, differentiated by day type. For a specific hour $h$ and day type $d$, the dependent variable $M_t$ for each grid $A$ is the observed value of the mixing index ($PMI_{A,t',m}$ or $MUI_{A,t'}$) for that specific hour.

**Supplementary Table 1 | Summary of explanatory variables and grid-level statistics.**

| Primary category | Subcategory | Sum value | Median value | Max value |
|---|---|---|---|---|
| Transport Facility | Airport | 9 | 1 | 6 |
| Transport Facility | Train Station | 334 | 1 | 102 |
| Transport Facility | Port | 63 | 1 | 7 |
| Transport Facility | Intercity Bus Station | 40 | 1 | 3 |

Continued on next page

**Supplementary Table 1 | Summary of explanatory variables and grid-level statistics (Continued).**

| Primary category | Subcategory | Sum value | Median value | Max value |
|---|---|---|---|---|
| Transport Facility | Subway Station | 1489 | 4 | 17 |
| Transport Facility | Bus Station | 6098 | 3 | 17 |
| Transport Facility | Parking Lot | 56628 | 13 | 278 |
| Transport Facility | Toll Station | 125 | 2 | 6 |
| Transport Facility | Highway Service | 19 | 2 | 2 |
| Transport networks (km) | Motorway | 2242.997 | 0 | 12.949 |
| Transport networks (km) | Primary roads | 1770.722 | 0 | 8.366 |
| Transport networks (km) | Secondary roads | 2222.137 | 0.3885 | 6.451 |
| Transport networks (km) | Tertiary roads | 4199.528 | 1.5375 | 11.193 |
| Transport networks (km) | Pedestrian roads | 6867.383 | 2.5405 | 18.555 |
| Roads diversity | Roads diversity | | 0.6276 | 0.9909 |

**Supplementary Table 2 | Regression coefficients explaining Probabilistic Mixing Index (PMI) and Multimodal Uniformity Index (MUI).** Columns 2-9 represent PMI models ($PMI_{A,t,m}$); Columns 10-11 represent MUI models ($MUI_{A,t}$). Significance levels: * $p < 0.1$, ** $p < 0.05$, *** $p < 0.001$. $R^2$ is the coefficient of determination, and MSE is the Mean Squared Error. Observations represent the number of grids included. Only significant variables are shown.

| Variable | Models for $PMI_{A,t,m}$ | | | | | | | | Models for $MUI_{A,t}$ | |
|---|---|---|---|---|---|---|---|---|---|---|
| | Active Mode | | Private Mode | | Bus Mode | | Railway Mode | | | |
| | Workday | Weekend | Workday | Weekend | Workday | Weekend | Workday | Weekend | Workday | Weekend |
| Motorway | 0.083$^{***}$ | 0.071$^{**}$ | 0.306$^{***}$ | 0.319$^{***}$ | 0.11$^{***}$ | 0.1$^{***}$ | -0.006 | -0.002 | -0.048$^{**}$ | -0.058$^{**}$ |
| Primary roads | 0.178$^{***}$ | 0.173$^{***}$ | 0.069$^{**}$ | 0.058$^{**}$ | 0.07$^{***}$ | 0.074$^{***}$ | -0.047$^{**}$ | -0.036$^{*}$ | 0.062$^{***}$ | 0.06$^{**}$ |
| Secondary roads | 0.13$^{***}$ | 0.115$^{***}$ | 0.037$^{*}$ | 0.017 | 0.012 | 0.003 | -0.02 | -0.012 | 0.046$^{***}$ | 0.046$^{***}$ |
| Tertiary roads | 0.309$^{***}$ | 0.258$^{***}$ | 0.211$^{***}$ | 0.148$^{***}$ | 0.157$^{***}$ | 0.082$^{***}$ | 0.079$^{***}$ | 0.058$^{**}$ | 0.107$^{***}$ | 0.108$^{***}$ |
| Pedestrian roads | -0.028 | -0.036 | -0.016 | -0.041$^{*}$ | -0.081$^{***}$ | -0.109$^{***}$ | 0.048$^{*}$ | 0.03 | 0.078$^{***}$ | 0.089$^{***}$ |
| Roads diversity | 0.059$^{**}$ | 0.069$^{***}$ | 0.17$^{***}$ | 0.2$^{***}$ | 0.062$^{***}$ | 0.063$^{***}$ | 0.119$^{***}$ | 0.101$^{***}$ | 0.145$^{***}$ | 0.167$^{***}$ |
| Bus Station | -0.011 | 0.032 | -0.058$^{**}$ | -0.044$^{*}$ | -0.045$^{*}$ | -0.035 | 0.037 | 0.036 | 0.253$^{***}$ | 0.262$^{***}$ |
| Airport | -0.078 | -0.141 | -0.084 | -0.177$^{**}$ | -0.092 | -0.163$^{*}$ | -0.005 | -0.005 | 0.043 | 0.053 |
| Subway Station | 0.283$^{***}$ | 0.262$^{***}$ | 0.039 | 0.018 | -0.003 | -0.041 | 0.104$^{***}$ | 0.087$^{***}$ | 0.316$^{***}$ | 0.306$^{***}$ |
| Observations | 2116 | 2112 | 2114 | 2108 | 1687 | 1684 | 334 | 334 | 2116 | 2115 |
| $R^2$ | 0.229 | 0.227 | 0.219 | 0.249 | 0.081 | 0.067 | 0.15 | 0.129 | 0.423 | 0.412 |
| MSE | 0.03 | 0.028 | 0.028 | 0.024 | 0.018 | 0.016 | 0.007 | 0.005 | 0.015 | 0.017 |

Prior to finalizing each OLS model, a systematic feature selection process is employed. We begin with the set of candidate transport infrastructure explanatory variables listed in Supplementary Table 1. The Variance Inflation Factor (VIF) is calculated for each variable to detect multicollinearity. Variables with a VIF ¿ 10 are iteratively removed until all remaining variables have acceptable VIFs ($\leq 10$), ensuring the robustness of the model estimates. The statistical results for the daily granularity models explaining both PMI and MUI are presented in Table 2. The results detailing the hourly variations in the influence of these transport variables on the mode-specific PMI are shown in Figs. 18–21, and those for the MUI are presented in Supplementary Fig. 22.

# 4 Agent-based model of individual mobility

This section provides detailed information about the agent-based mobility model used to simulate travel mode choices and their impact on the structure of social encounter opportunities. The model is grounded in discrete choice theory [14] and simulates the behavior of individuals commuting from home to work during morning peak hours (9:00-10:00 AM).

## 4.1 Model specification

The model considers a population of individuals, each belonging to a specific income group $g \in \mathcal{G}$ (where $|\mathcal{G}| = 4$). Each individual $i$ needs to make a trip from their home location to their workplace. For this commute, they choose a travel mode $m$ from a set of available modes $\mathcal{M} = \{\text{active, private, railway}\}$. The choice is probabilistic and assumes individuals aim to minimize their perceived travel cost $\mathcal{C}_{gm}$. The probability $p_{gm}$ that an individual from group $g$ chooses mode $m$ is given by the multinomial logit formula:

$$p_{gm} = \frac{\exp(-\delta \mathcal{C}_{gm})}{\sum_{m' \in \mathcal{M}} \exp(-\delta \mathcal{C}_{gm'})}, \tag{S7}$$

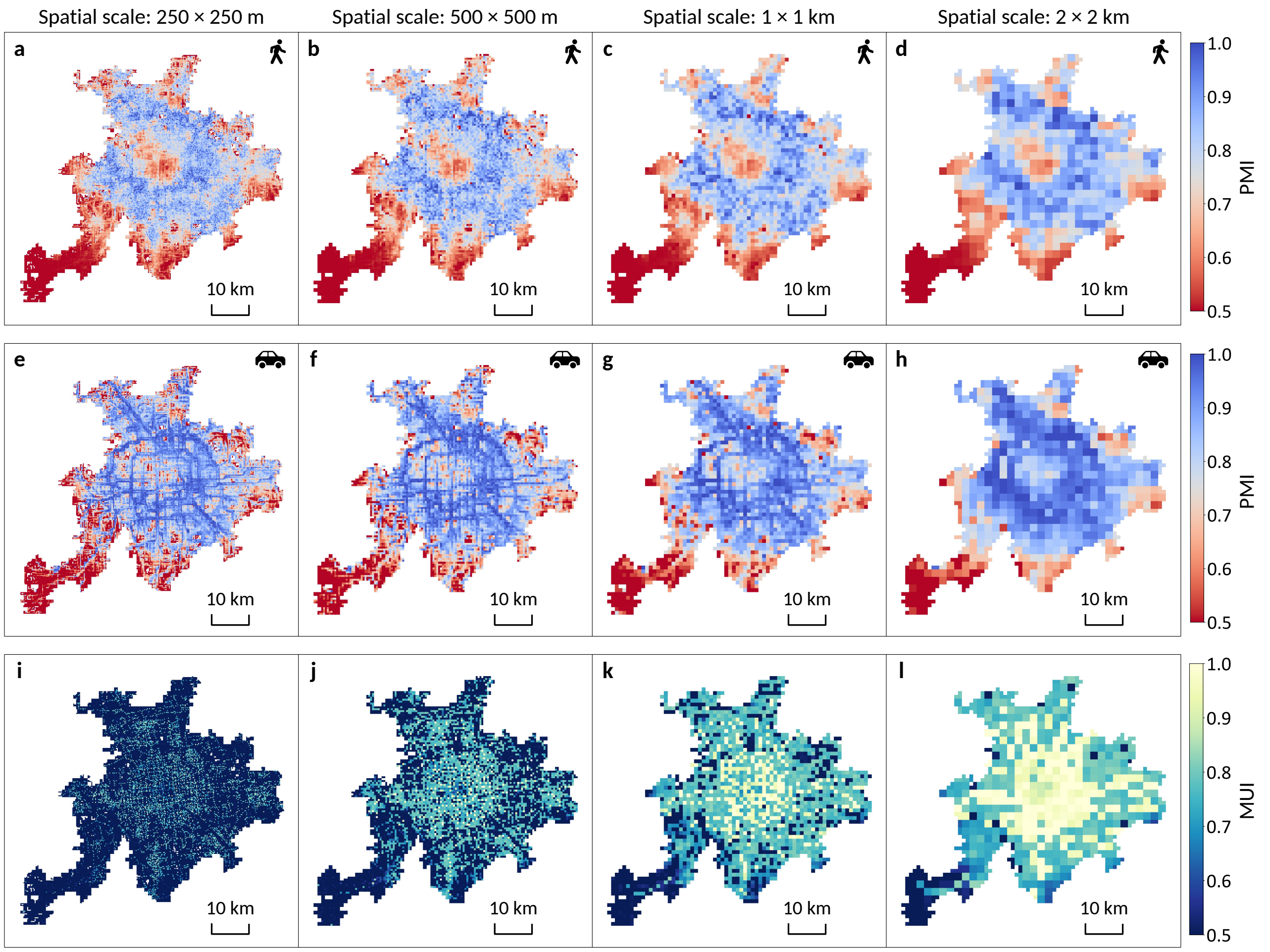


**Supplementary Figure 17 | Illustration of PMI and MUI distributions at different spatial scales in the Beijing metropolitan area.**

where $\delta$ is the sensitivity parameter, reflecting how strongly cost differences influence mode choice. The perceived travel cost $\mathcal{C}_{gm}$ is defined as:

$$\mathcal{C}_{gm} = (\alpha_g + \beta_m)T_m, \tag{S8}$$

where:

- $T_m$ is the estimated travel time for mode $m$. This is calculated as the duration of the shortest path $\mathbf{R}_m$ from an individual's home to workplace using the real-world transport networks in the Beijing metropolitan area.
- $\alpha_g$ represents the monetary value of time for income group $g$.
- $\beta_m$ represents other mode-specific cost components (monetary and non-monetary) per unit of travel time.

The model assumes that individuals have perfect information about travel times and costs. It also inherently includes the Independence of Irrelevant Alternatives (IIA) property common to logit models [15]. The model output consists of the mode choice probabilities $p_{gm}$. These probabilities, combined with the shortest travel paths $\mathbf{R}_m$, are used as inputs to calculate the mode-specific Probabilistic Mixing Index (PMI), as described in the main text.

## 4.2 Parameter calibration

The model parameters include the sensitivity parameter $\delta$, the group-specific value of time parameters $\alpha_g$, and the mode-specific cost factors $\beta_m$. The relative values of $\alpha_g$ are determined a priori based on the average income of each group, following the economic principle that the value of time correlates with income [16]. This yields $\alpha_1 = 0.203, \alpha_2 = 0.349, \alpha_3 = 0.596$, and $\alpha_4 = 1$. The main calibration process then focuses on estimating the remaining four parameters: $\delta$, $\beta_{\text{active}}$, $\beta_{\text{private}}$, and $\beta_{\text{railway}}$. The objective is to minimize the discrepancy between model-predicted mode-specific mixing index (PMI) values and empirically observed PMI values from mobile phone data during workday morning peak hours (9:00-10:00 AM).

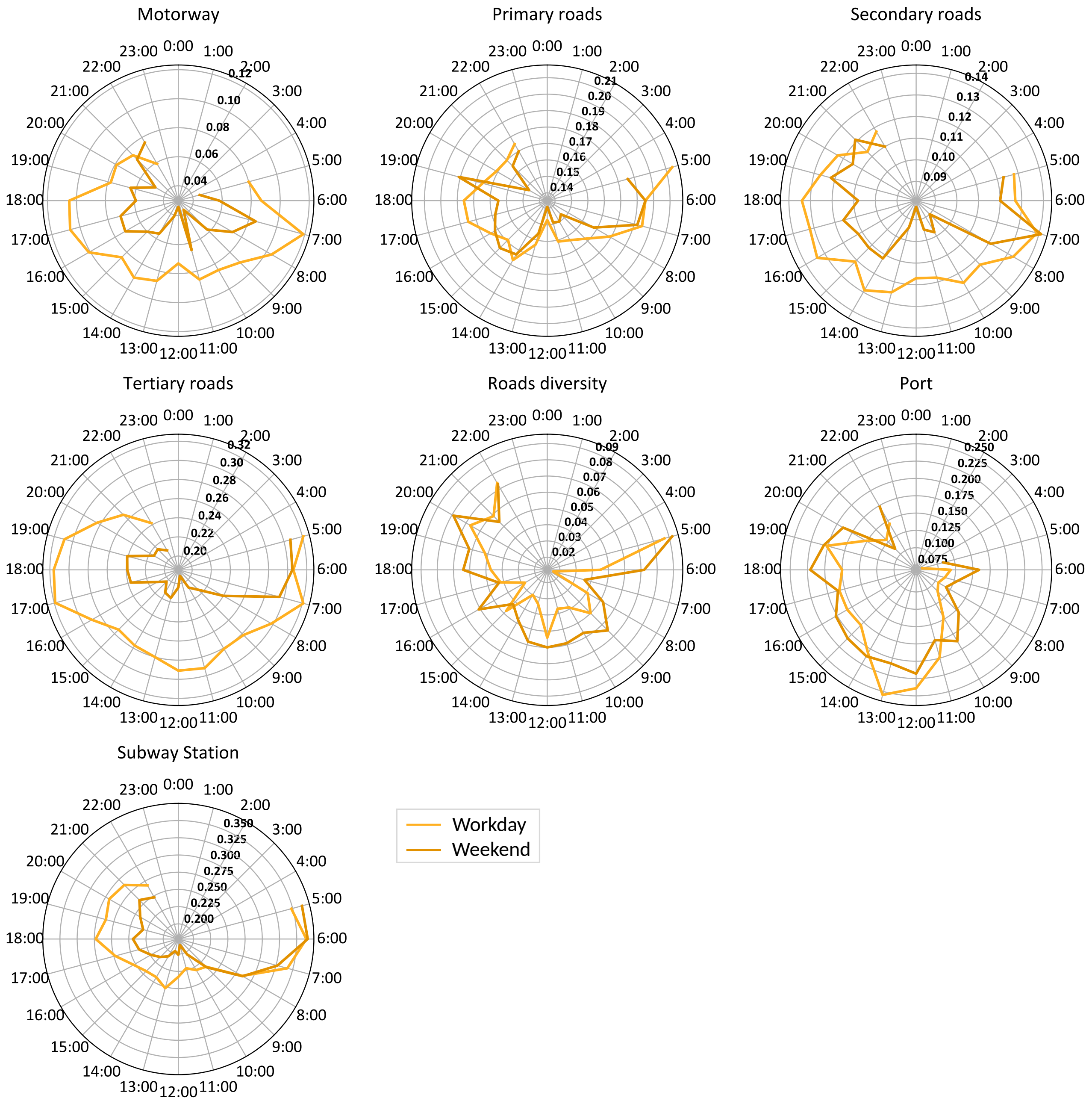


**Supplementary Figure 18 | Hourly PMI dynamics for active mode across workdays and weekends.** Each panel visualizes the hourly variation of the regression coefficients for a specific explanatory variable. Only statistically significant variables are displayed.

To perform this calibration, we define an objective function $L(\Theta')$ that quantifies the goodness-of-fit. We use the sum of squared errors (SSE) across all relevant spatial units $s$ for each mode $m$:

$$L(\delta, \beta_{\text{active}}, \beta_{\text{private}}, \beta_{\text{railway}}) = \sum_{m \in \mathcal{M}} \sum_{s \in S_m} \left( \widehat{PMI}_{s,t,m}(\Theta') - PMI^{\text{obs}}_{s,t,m} \right)^2, \tag{S9}$$

where $\widehat{PMI}_{s,t,m}(\Theta')$ is the model-predicted mixing index value and $PMI^{\text{obs}}_{s,t,m}$ is the corresponding empirically observed value. We employ a Grid Search approach to find the parameter set that minimizes this objective function.

The model simulation is executed for each combination of parameter values in the grid. The parameter combination yielding the minimum value of the objective function is selected as the optimal calibrated parameter set. The resulting calibrated parameter values are: $\delta^* = 3 \times 10^{-4}$, $\beta^*_{\text{active}} = 0.22$, $\beta^*_{\text{private}} = 2.1$, and $\beta^*_{\text{railway}} = 0.07$.

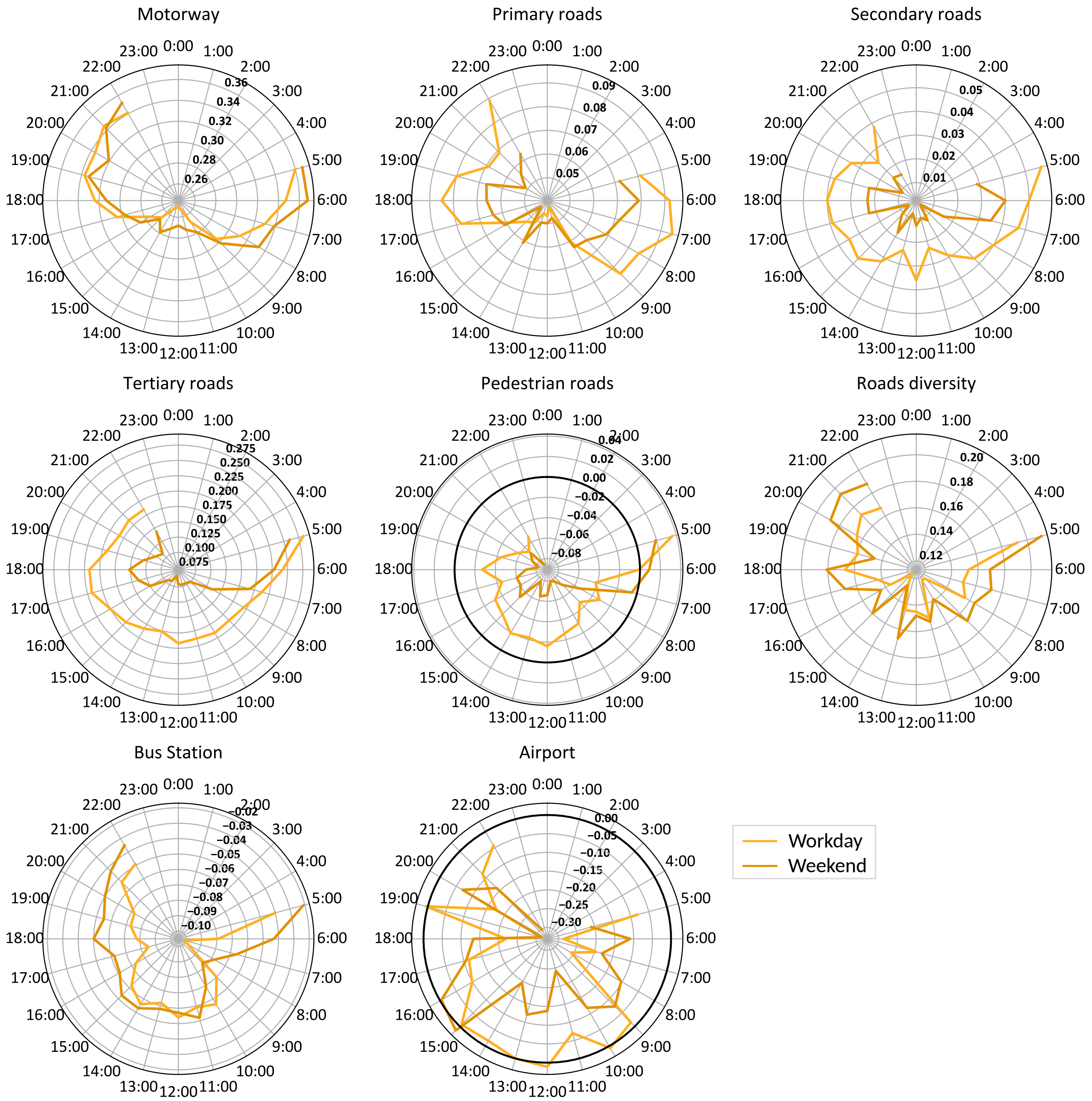


**Supplementary Figure 19 | Hourly PMI dynamics for private mode across workdays and weekends.** Each panel visualizes the hourly variation of the regression coefficients for a specific explanatory variable. Only statistically significant variables are displayed.

To assess the model's performance, we compare the model-predicted PMI values with the empirically observed PMI values for each spatial unit. A strong positive correlation, quantified by Pearson correlation coefficients (active: $r = 0.9327^{***}$; private: $r = 0.9613^{***}$; railway: $r = 0.9551^{***}$; see Supplementary Fig. 23), demonstrates a good fit of the model to the observed patterns of encounter diversity.

## 4.3 Simulation for private car use control policies

A central challenge in urban transport planning is designing policies that achieve collective goals without exacerbating existing social inequalities [17]. The distributional effects of transport policies are a critical consideration [18]. This study investigates these effects by simulating the impacts of urban transport policies on patterns of encounter diversity and social equity. Measures controlling private car usage, such as congestion pricing [19, 20], fuel taxes [21, 22], or parking regulations [23], are prominent tools for managing urban mobility.

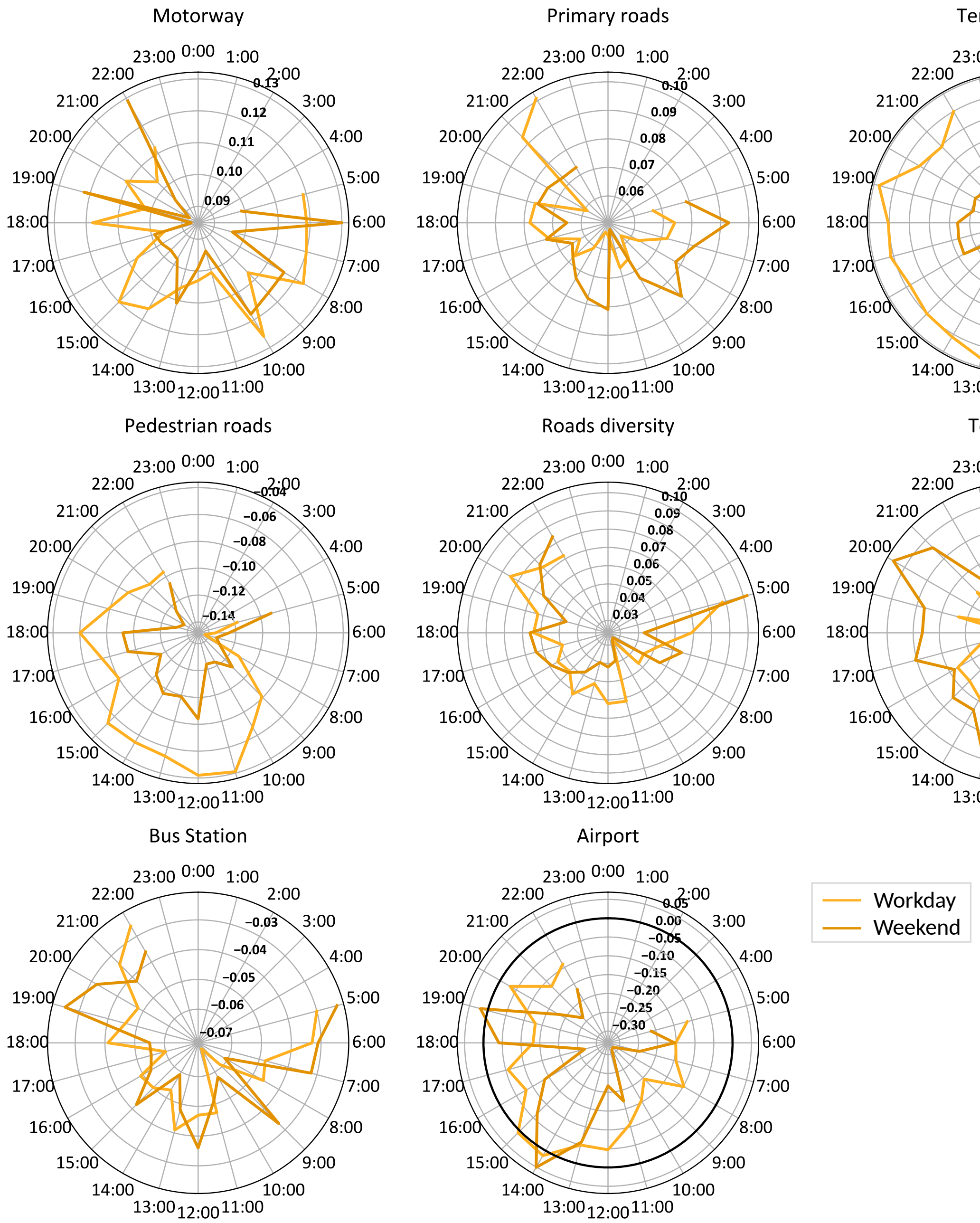


**Supplementary Figure 20 | Hourly PMI dynamics for bus mode across workdays and weekends.** Each panel visualizes the hourly variation of the regression coefficients for a specific explanatory variable. Only statistically significant variables are displayed.

We operationalize these policies by systematically increasing the mode-specific cost parameter $\beta_{\text{private}}$, representing a higher generalized cost of driving. We explore the sensitivity of travel behavior and patterns of encounter diversity to such interventions. We implement two simulation scenarios: (1) **Uniform citywide cost increase** ($\beta'_{\text{private}} = \beta^*_{\text{private}} + \Delta\beta_{\text{private}}$ for all trips) and (2) **Downtown-targeted cost increase** (cost increase only for trips with an origin or destination downtown). For both scenarios, we vary the cost increment, $\Delta\beta_{\text{private}}$, from 0 to 15. For each value, we recalculate perceived travel costs, mode choice probabilities, and the resultant mode-specific mixing potential (PMI), changes in mode shares, and average travel costs per income group.

For the first scenario, increasing the citywide cost of driving reduces private car use and shifts commuters to other modes, leading to complex changes in mixing potential across modes. To illustrate the spatial impact, we select $\Delta\beta_{\text{private}} = 5$. The spatial distribution of changes is visualized in Supplementary Fig. 24. The policy reduces the overall mixing potential among private car users. Conversely, for active and railway travel, mixing potential increases in the suburbs and decreases in the downtown core.

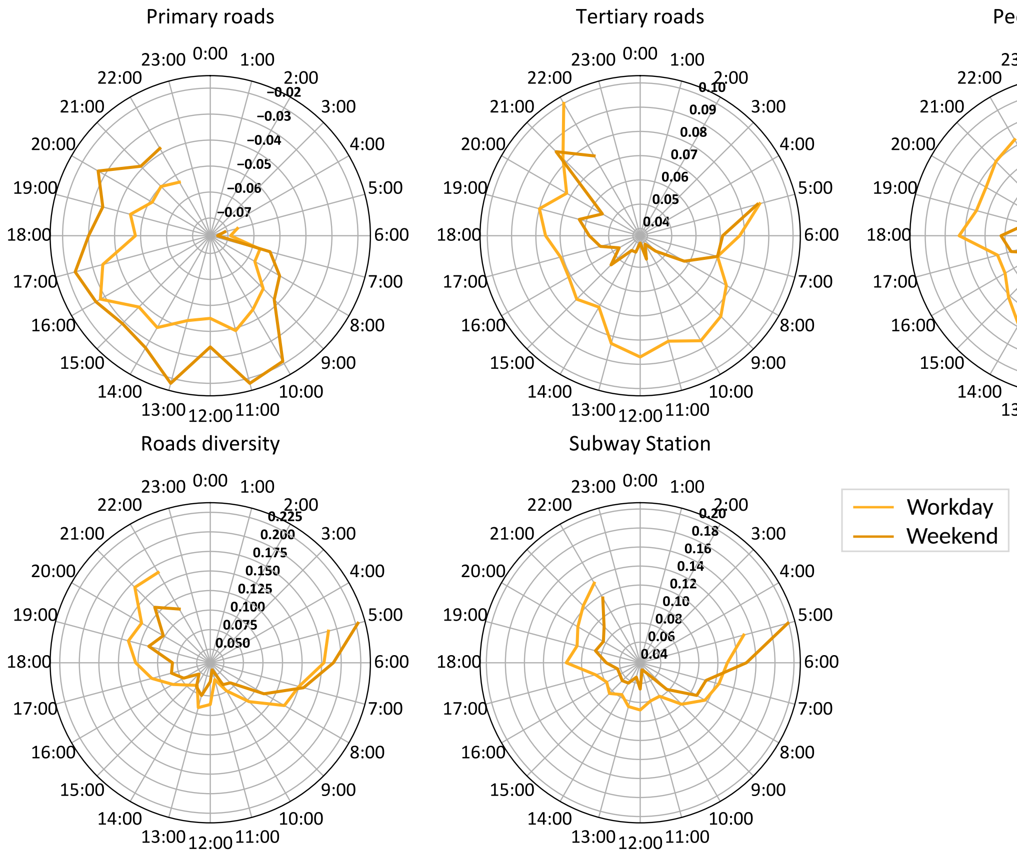


**Supplementary Figure 21 | Hourly PMI dynamics for railway mode across workdays and weekends.** Each panel visualizes the hourly variation of the regression coefficients for a specific explanatory variable. Only statistically significant variables are displayed.

For the second scenario (downtown-targeted), the policy has a smaller impact on lower-income groups, as fewer of them commute to the restricted zone (Supplementary Fig. 25 and Fig. 26). This leads to a higher overall PMI for private car travel citywide, indicating increased mixing potential among remaining users (Supplementary Fig. 27). Conversely, for active and railway modes, the overall citywide PMI decreases, signaling reduced mixing potential.

In summary, the spatial design of private car control policies fundamentally alters their distributional effects. A uniform policy spreads the burden broadly but yields mixed results on mixing potential. A downtown-targeted policy concentrates costs but paradoxically increases mixing potential for private cars while reducing it for other modes. These outcomes highlight critical trade-offs between travel costs and social mixing. Policymakers must consider both cost burdens and impacts on encounter diversity across all modes.

## 4.4 Simulation for public transport subsidy policies

Promoting public transport through subsidies is a common strategy for influencing travel behavior and addressing equity concerns [24, 25]. We simulate this by reducing the railway cost parameter $\beta_{\text{railway}}$. We introduce a subsidy factor $\Delta\beta_{\text{public}}$ and modify the cost parameter as $\beta'_{\text{railway}} = \beta^*_{\text{railway}} + \Delta\beta_{\text{public}}$, varying $\Delta\beta_{\text{public}}$ from 0 to -0.07. For each subsidy level, we recalculate mode choice probabilities, average travel costs, and mode-specific mixing potential (PMI).

The results confirm a shift towards railway usage, with lower-income individuals exhibiting a larger response (Supplementary Fig. 28a-c). This translates into greater travel cost savings for them (Supplementary Fig. 29). However, the impact on mode-specific mixing potential is complex. The influx of predominantly lower-income users onto the railway reduces mixing potential within that mode (lower PMI, Supplementary Fig. 28f). Similarly, as users shift from private cars, the remaining pool of drivers becomes less diverse, also reducing mixing potential (lower PMI, Supplementary Fig. 28e). Conversely, the active travel mode experiences increased mixing potential (higher PMI, Supplementary Fig. 28d). The magnitude of these changes is relatively small, suggesting diminishing returns from further fare-based subsidies.

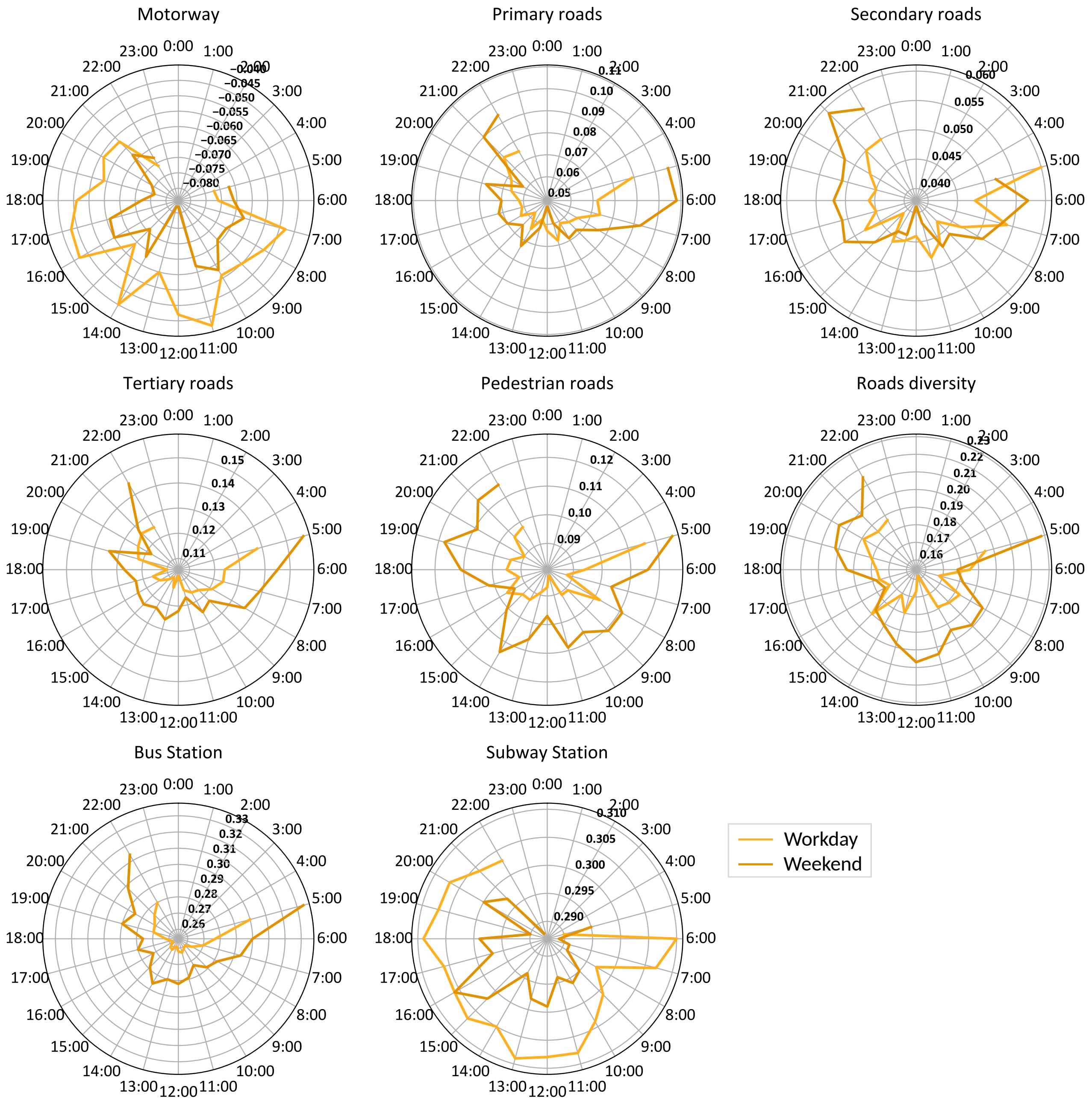


**Supplementary Figure 22 | Hourly MUI dynamics across workdays and weekends.** Each panel visualizes the hourly variation of the regression coefficients for a specific explanatory variable. Only statistically significant variables are displayed.

The spatial analysis (Supplementary Fig. 30) shows that for the private mode, the policy tends to reduce mixing potential in downtown areas. For active travel, mixing potential increases in the suburbs but decreases downtown. The railway mode exhibits complex spatial effects without a clear regional pattern. These findings suggest that while subsidies reduce travel costs, they can inadvertently reduce mixing potential within the subsidized mode and among users of other modes.

## 4.5 Simulation for promoting active travel policies

We explore the distributional impacts of policies promoting active travel, which can yield co-benefits like improved health and reduced emissions. Strategies often involve improving infrastructure [26], traffic calming [27], or public campaigns [28]. We model these policies by reducing the cost parameter $\beta_{\text{active}}$. We introduce a policy variable $\Delta\beta_{\text{active}}$ and vary it from 0 to -0.44. As before, we recalculate the mixing potential (PMI), mode usage shifts, and average travel costs.

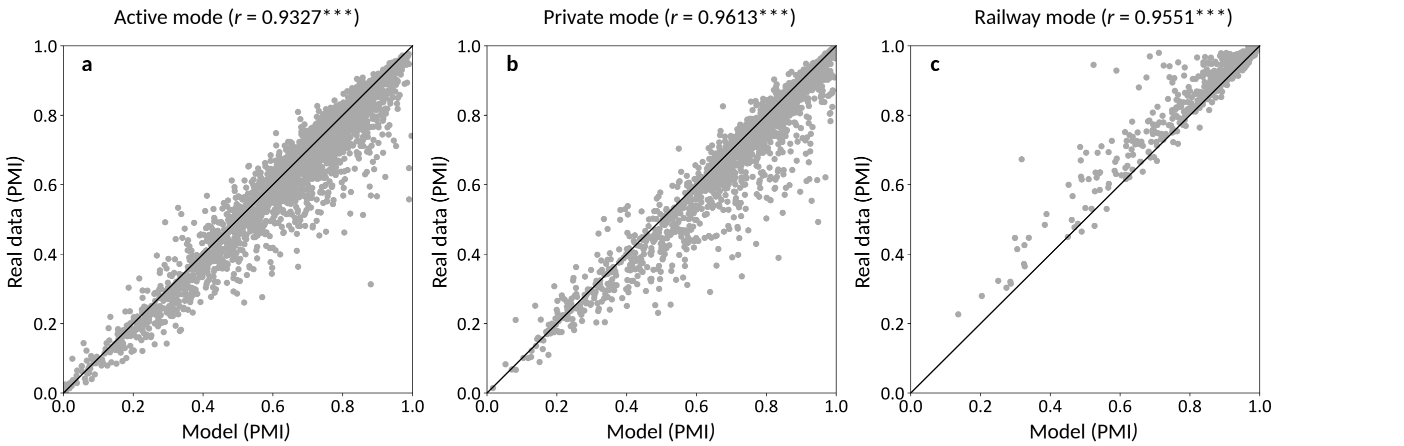


**Supplementary Figure 23 | Comparison of model-predicted and observed PMI values.** Scatter plots showing the relationship between predicted PMI (using calibrated parameters) and observed PMI for spatial units during the 9:00-10:00 AM peak hour, for (**a**) Active, (**b**) Private, and (**c**) Railway modes. Pearson correlation coefficients (r) are indicated ($^{***}p < 0.001$).

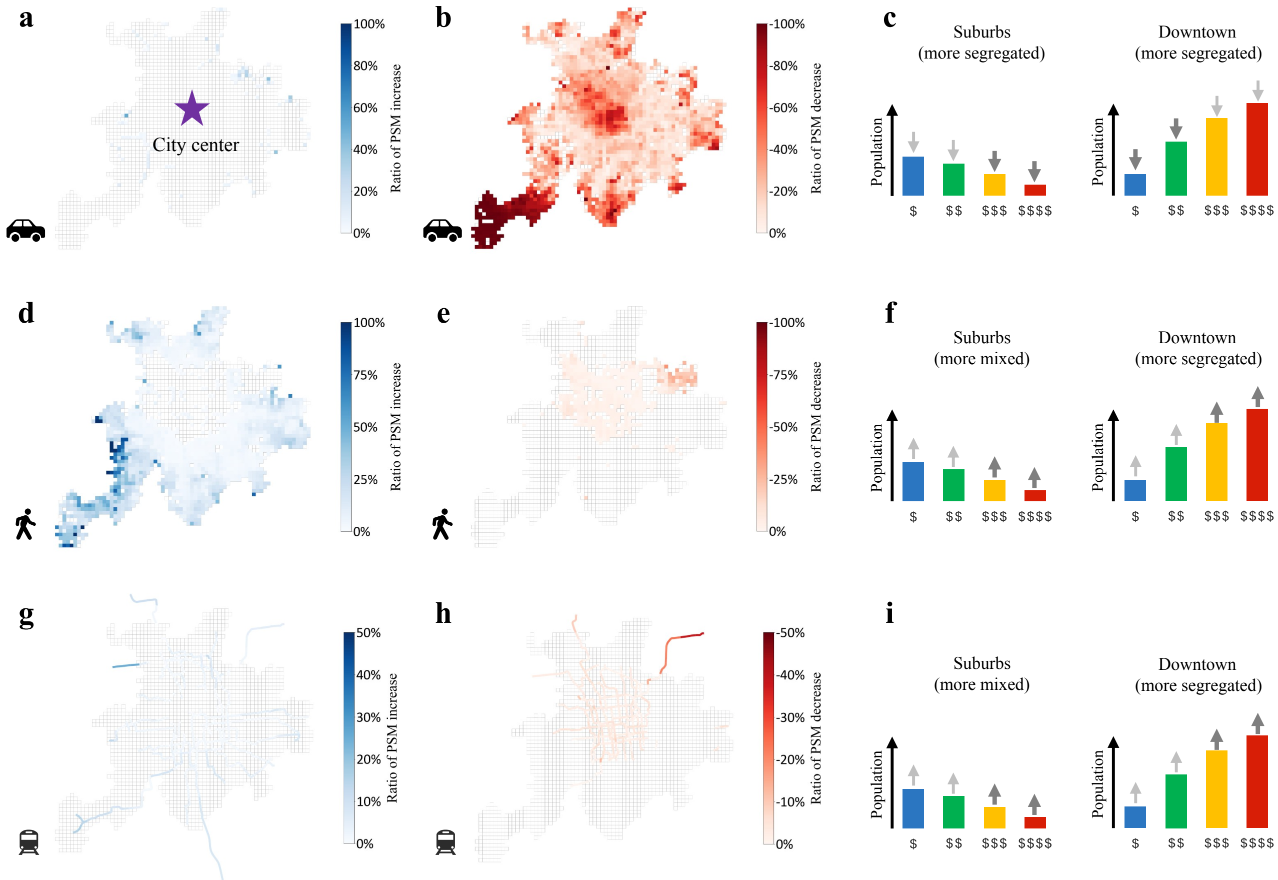


**Supplementary Figure 24 | Spatial distribution of changes in the Probabilistic Mixing Index (PMI) for three transport modes under a uniform private car cost increase policy.** The figure compares the policy scenario ($\Delta\beta_{\text{private}} = 5$) to the baseline. Panels show spatial units where PMI increased (indicating increased mixing potential) or decreased (indicating reduced mixing potential). Other panels illustrate policy-induced shifts in mode usage by income group.

Promoting active travel shows progressive distributional effects, disproportionately benefiting lower-income groups with the largest travel cost savings (Supplementary Fig. 31a-c and Fig. 32). However, the impacts on encounter diversity are multifaceted. While citywide mixing potential generally increases for active and private

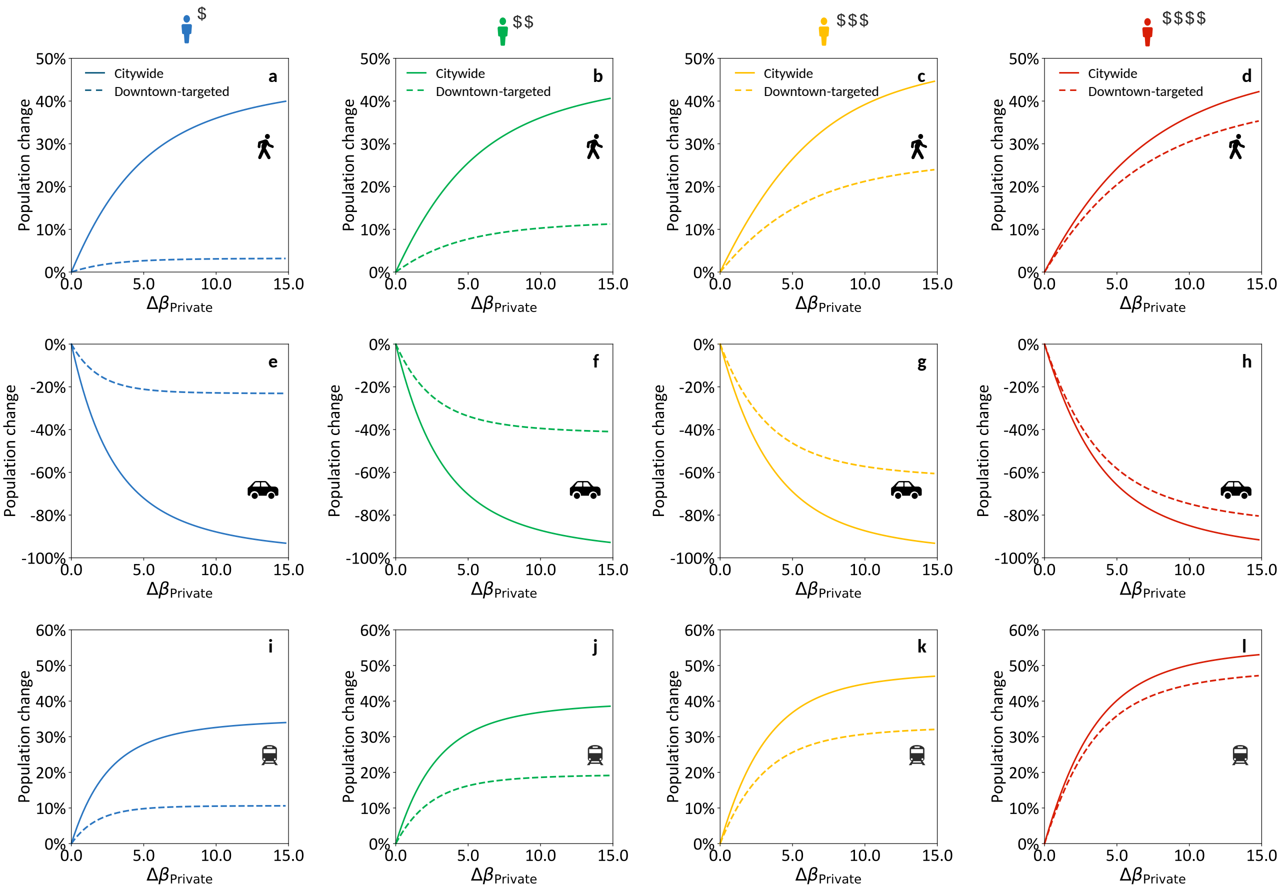


**Supplementary Figure 25 | Proportional changes in mode usage by income groups under two private car policy scenarios.**

modes (Supplementary Fig. 31d-f), the spatial effects diverge significantly (Supplementary Fig. 33). Active travel promotes income mixing downtown but reduces it in suburbs. Conversely, private and railway modes see their mixing potential decrease downtown while it improves in suburbs. This highlights a key trade-off: promoting active travel reshapes patterns of encounter diversity in complex, spatially dependent ways. Policymakers should consider complementary measures to ensure fairer social outcomes across all modes and areas.

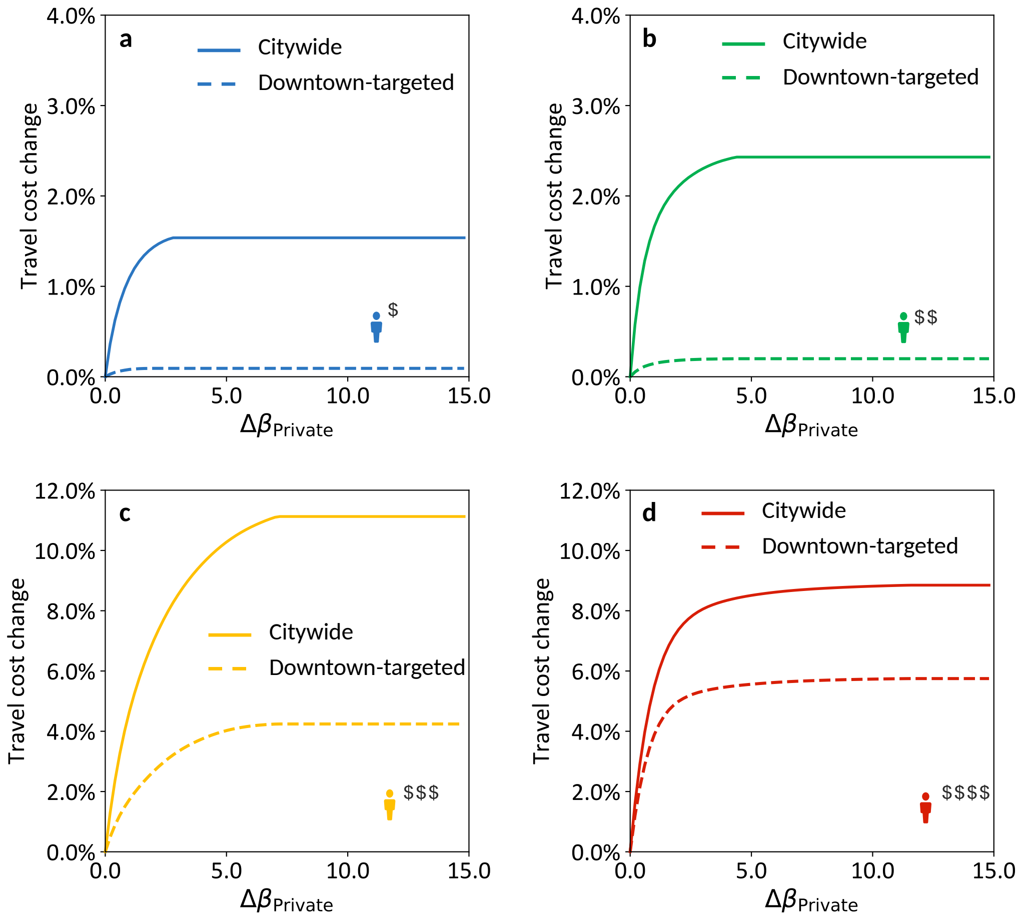


**Supplementary Figure 26 | Impact of two private car policies on average travel costs by income group.**

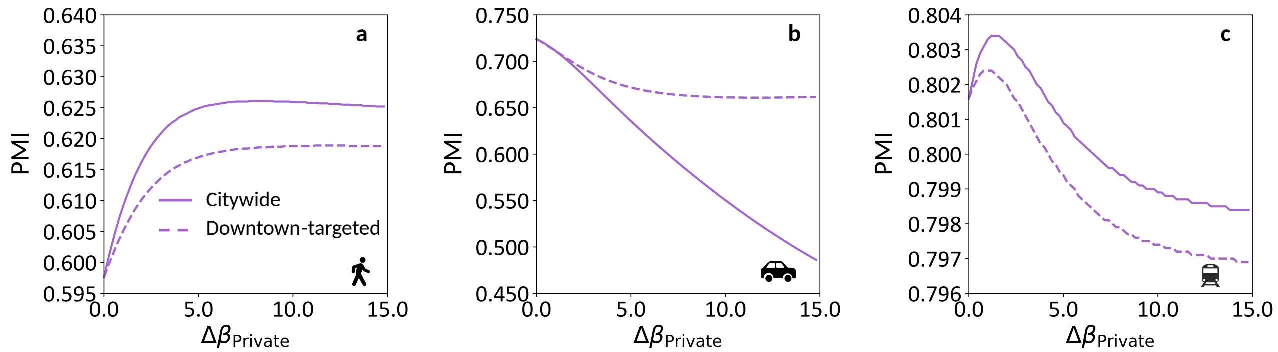


**Supplementary Figure 27 | Impact of two private car policies on citywide mixing potential by mode.** Under the downtown-targeted policy, overall mixing potential increases for private car users (higher PMI) while it decreases for both active and railway users (lower PMI).

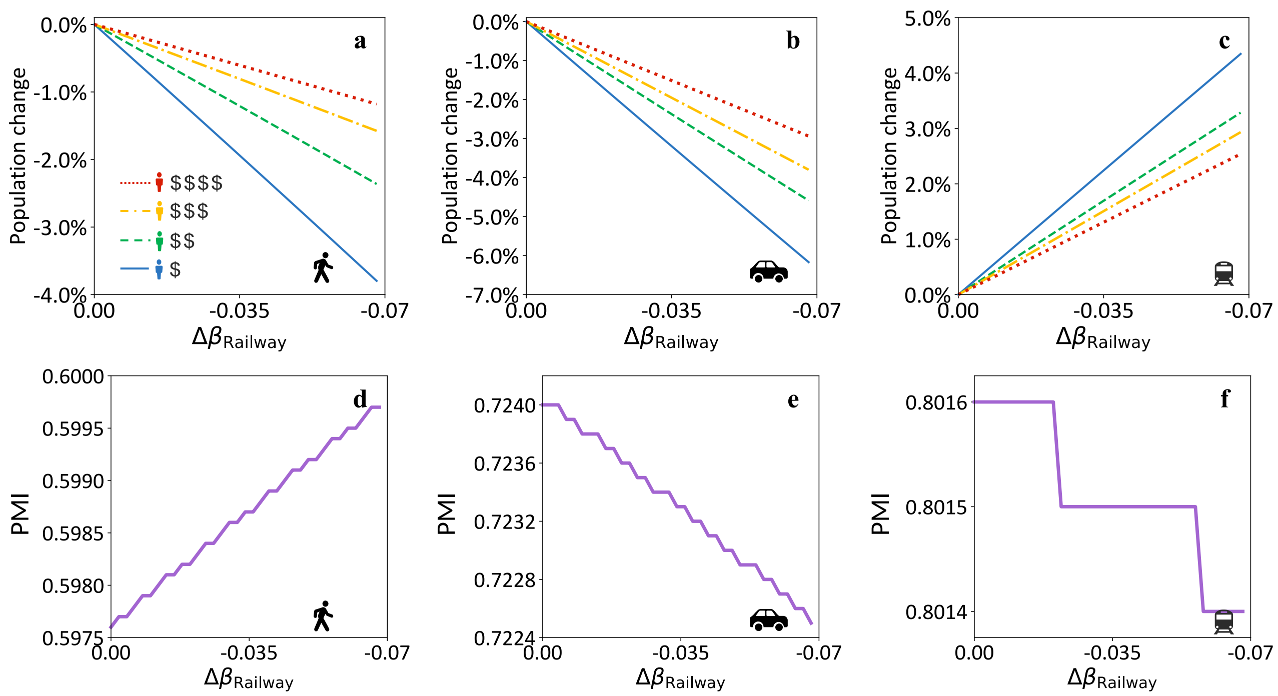


**Supplementary Figure 28 | Impact of public transport subsidies on mode usage and citywide mixing potential. a–c** Proportional changes in mode usage by income group. **d–f** Overall citywide mixing potential (PMI) for each mode. Results indicate increased mixing potential (increasing PMI) for active travel, but reduced mixing potential (decreasing PMI) for both private and railway travel.

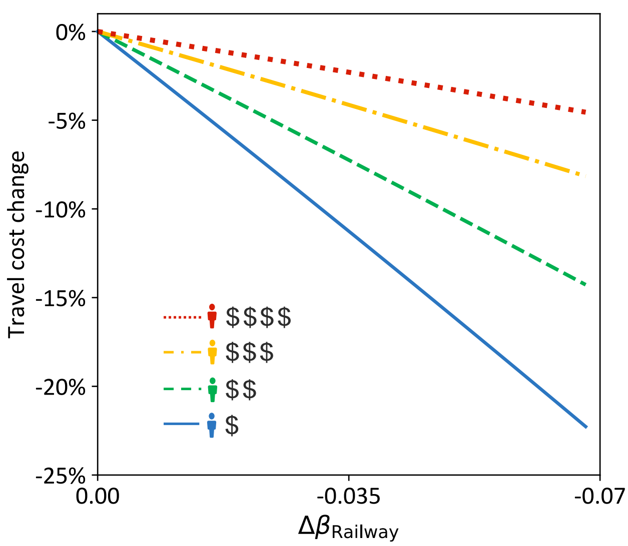


**Supplementary Figure 29 | Impact of public transport subsidies on average travel costs by income group.**

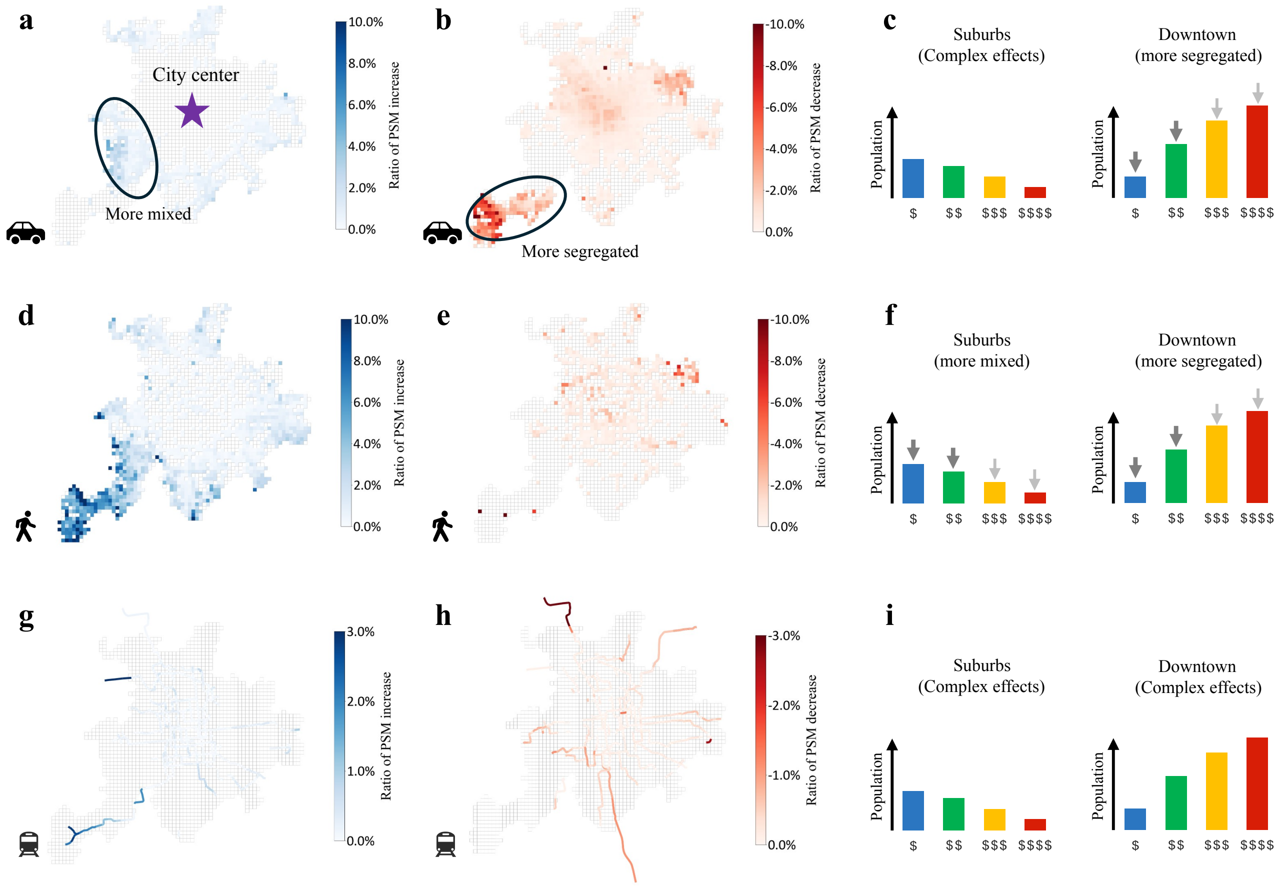


**Supplementary Figure 30 | Spatial distribution of changes in the Probabilistic Mixing Index (PMI) for three transport modes under public transport subsidy policies.** The figure compares the maximum subsidy scenario to the baseline. Panels show where PMI increased (increased mixing potential) or decreased (reduced mixing potential), with illustrations of mode shifts.

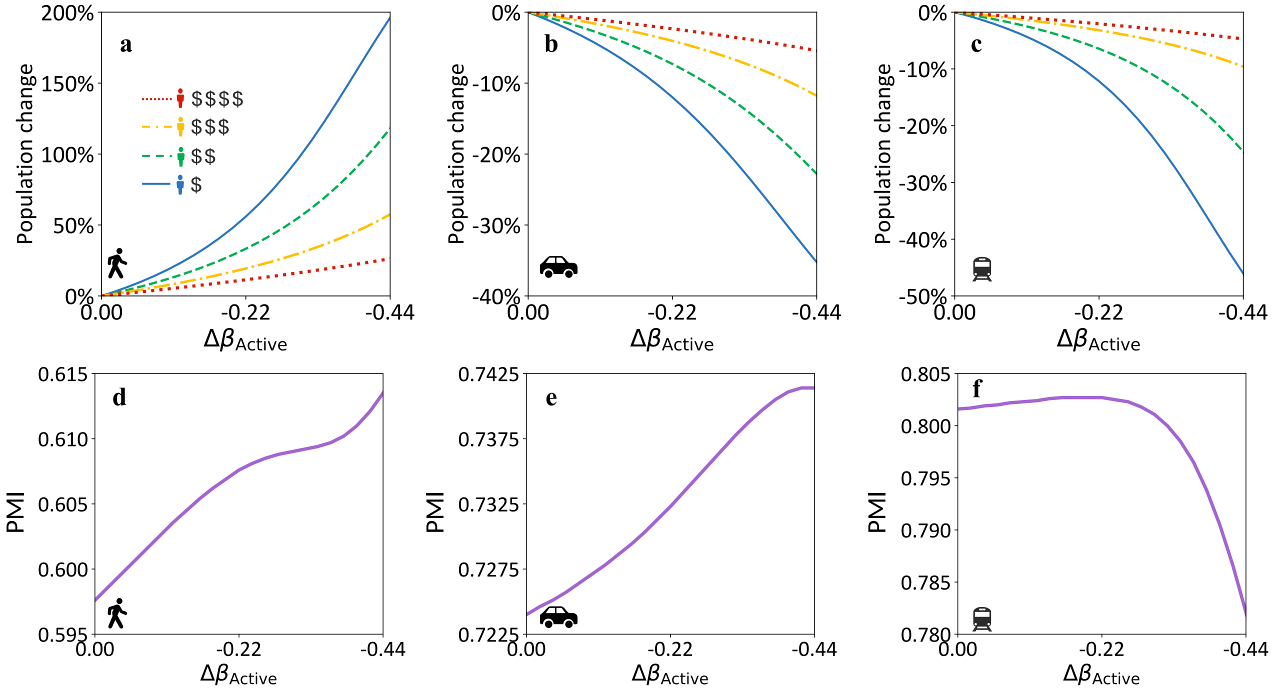


**Supplementary Figure 31 | Impact of promoting active travel policies on mode usage and citywide mixing potential. a–c** Proportional changes in mode usage by income group. **d–f** Overall citywide mixing potential (PMI) for each mode.

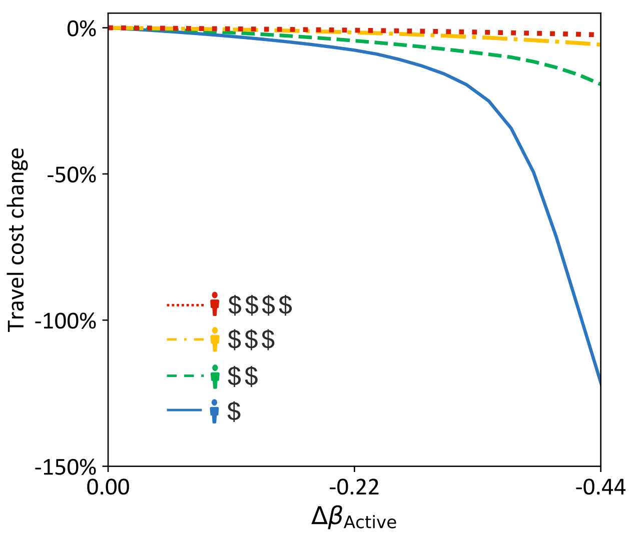


**Supplementary Figure 32 | Impact of promoting active travel policies on average travel costs by income group.**

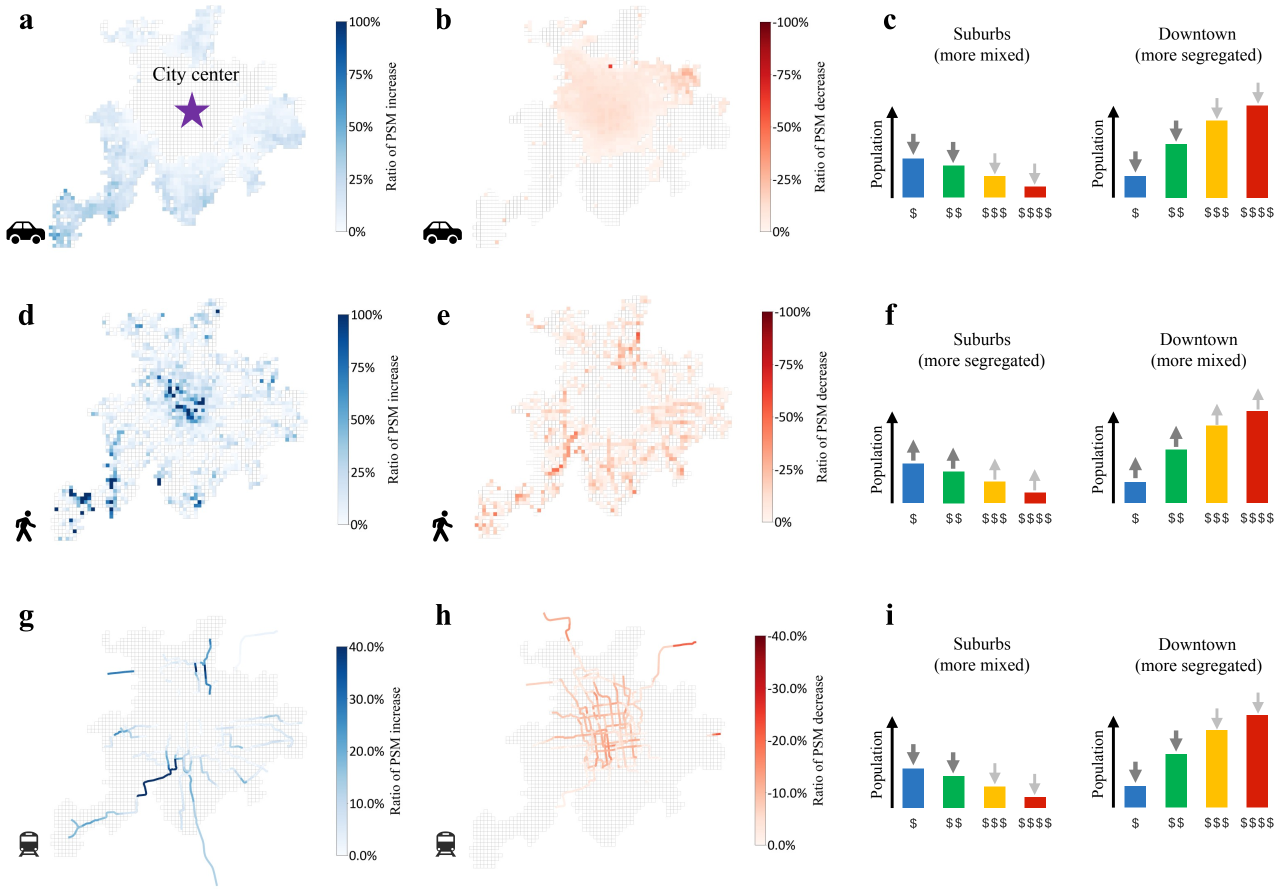


**Supplementary Figure 33 | Spatial distribution of changes in the Probabilistic Mixing Index (PMI) for three transport modes under active travel policies.** The figure compares the maximum promotion scenario to the baseline. Panels show where PMI increased (increased mixing potential) or decreased (reduced mixing potential), with illustrations of mode shifts.

# Supplementary references


[1] Ester, M., Kriegel, H.-P., Sander, J. & Xu, X. A density-based algorithm for discovering clusters in large spatial databases with noise. *Proceedings of the Second International Conference on Knowledge Discovery and Data Mining (KDD)* 226–231 (1996).

[2] National Bureau of Statistics of China. The seventh national population census (2021). https://www.stats.gov.cn/english/PressRelease/202105/t20210510_1817185.html.

[3] Beijing Municipal Bureau of Statistics. Beijing statistical yearbook 2020 (2020). https://nj.tjj.beijing.gov.cn/nj/main/2020-tjnj/zk/e/indexee.html.

[4] Beijing Municipal Bureau of Statistics. Beijing statistical yearbook 2021 (2021). https://nj.tjj.beijing.gov.cn/nj/main/2021-tjnj/zk/e/indexee.htm.

[5] Beijing Municipal Bureau of Statistics. Beijing statistical yearbook 2022 (2022). https://nj.tjj.beijing.gov.cn/nj/main/2022-tjnj/zk/e/indexee.htm.

[6] Beijing Municipal Bureau of Statistics. Beijing statistical yearbook 2023 (2023). https://nj.tjj.beijing.gov.cn/nj/main/2023-tjnj/zk/e/indexee.htm.

[7] Deville, P. *et al.* Dynamic population mapping using mobile phone data. *Proceedings of the National Academy of Sciences* **111**, 15888–15893 (2014).

[8] Zheng, Y., Zhang, L., Xie, X. & Ma, W.-Y. Mining interesting locations and travel sequences from GPS trajectories. *Proceedings of the 18th International Conference on World Wide Web* 791–800 (2009).

[9] Hanley, J. A. & McNeil, B. J. The meaning and use of the area under a receiver operating characteristic (ROC) curve. *Radiology* **143**, 29–36 (1982).

[10] Brier, G. W. Verification of forecasts expressed in terms of probability. *Monthly Weather Review* **78**, 1–3 (1950).

[11] Amap navigation application API. https://lbs.amap.com/. Accessed on May 2024.

[12] Cai, Z. *et al.* MemDA: Forecasting urban time series with memory-based drift adaptation. *Proceedings of the 32nd ACM International Conference on Information and Knowledge Management* 193–202 (2023).

[13] Kolmogorov, A. Sulla determinazione empirica di una legge di distribuzione. *Giornale dell'Istituto Italiano degli Attuari* **4**, 83–91 (1933).

[14] Ben-Akiva, M. & Lerman, S. R. *Discrete Choice Analysis: Theory and Application to Travel Demand* (MIT Press, Cambridge, MA, 1985).

[15] McFadden, D. *Conditional Logit Analysis of Qualitative Choice Behavior* (Academic Press, New York, 1974).

[16] Becker, G. S. A theory of the allocation of time. *The Economic Journal* **75**, 493–517 (1965).

[17] Lucas, K. Transport and social exclusion: Where are we now? *Transport Policy* **20**, 105–113 (2012).

[18] Pereira, R. H. M., Schwanen, T. & Banister, D. Distributive justice and equity in transportation. *Transport Reviews* **37**, 170–191 (2017).

[19] Leape, J. The london congestion charge. *Journal of Economic Perspectives* **20**, 157–176 (2006).

[20] Eliasson, J. A cost–benefit analysis of the stockholm congestion charging system. *Transportation Research Part A: Policy and Practice* **43**, 468–480 (2009).

[21] Goodwin, P., Dargay, J. & Hanly, M. Elasticities of road traffic and fuel consumption with respect to price and income: a review. *Transport Reviews* **24**, 275–292 (2004).

[22] Parry, I. W. H., Walls, M. & Harrington, W. Automobile externalities and policies. *Journal of Economic Literature* **45**, 373–399 (2007).

[23] Marsden, G. The evidence base for parking policies—a review. *Transport Policy* **13**, 447–457 (2006).

[24] Taylor, B. D. Rethinking transit policy in an era of budgetary constraint: Who benefits from transit subsidies? *Transportation Research Record* **1804**, 93–100 (2002).

[25] Pucher, J. & Buehler, R. Making public transport financially sustainable. *Transport Policy* **15**, 241–254 (2008).

[26] Pucher, J., Dill, J. & Handy, S. Infrastructure, programs, and policies to increase bicycling: An international review. *Preventive Medicine* **50**, S106–S125 (2010).

[27] Bunn, F. *et al.* Area-wide traffic calming for preventing traffic related injuries. *Cochrane Database of Systematic Reviews* (2003).

[28] Cairns, S. *et al.* Smarter choices: assessing the potential to achieve traffic reduction using 'soft measures'. *Transport Reviews* **28**, 593–618 (2008).